Monthly Notices
of the
ROYAL ASTRONOMICAL SOCIETY

MNRAS **449,** 1309–1326 (2015) doi:10.1093/mnras/stv338

The nuclear and extended infrared emission of the Seyfert galaxy NGC 2992 and the interacting system Arp 245

I. García-Bernete,[1,2]★ C. Ramos Almeida,[1,2]† J. A. Acosta-Pulido,[1,2]
A. Alonso-Herrero,[3,4] M. Sánchez-Portal,[5] M. Castillo,[5] M. Pereira-Santaella,[6]
P. Esquej,[7] O. González-Martín,[1,2,8] T. Díaz-Santos,[9,10] P. Roche,[11] S. Fisher,[12]
M. Pović,[13] A. M. Pérez García,[1,2] I. Valtchanov,[5] C. Packham[4] and N. A. Levenson[14]

[1]*Instituto de Astrofísica de Canarias, Calle Vía Láctea, s/n, E-38205 La Laguna, Tenerife, Spain*
[2]*Departamento de Astrofísica, Universidad de La Laguna, E-38206 La Laguna, Tenerife, Spain*
[3]*Instituto de Física de Cantabria, CSIC-Universidad de Cantabria, E-39005 Santander, Spain*
[4]*Department of Physics and Astronomy, University of Texas at San Antonio, One UTSA Circle, San Antonio, TX 78249, USA*
[5]*Heschel Science Centre, ESAC, Villanueva de la Cañada, E-28691 Madrid, Spain*
[6]*Centro de Astrobiología, CSIC-INTA, Torrejón de Ardoz, E-28850 Madrid, Spain*
[7]*Departamento de Astrofísica, Facultad de CC. Físicas, Universidad Complutense de Madrid, E-28040 Madrid, Spain*
[8]*Centro de Radioastronomía y Astrofísica (CRyA-UNAM), 3-72 (Xangari), 8701 Morelia, Mexico*
[9]*Spitzer Science Center, California Institute of Technology, MS 220-6, Pasadena, CA 91125, USA*
[10]*Núcleo de Astronomía de la Facultad de Ingeniería, Universidad Diego Portales, Av. Ejército Libertador 441, Santiago, Chile*
[11]*Department of Physics, University of Oxford, Oxford OX1 3RH, UK*
[12]*Department of Physics, University of Oregon, Eugene, OR 97401, USA*
[13]*Instituto de Astrofísica de Andalucía (IAA-CSIC), E-18008 Granada, Spain*
[14]*Gemini Observatory, Casilla 603, La Serena, Chile*

Accepted 2015 February 13. Received 2015 February 12; in original form 2014 November 14

ABSTRACT

We present subarcsecond resolution infrared (IR) imaging and mid-IR (MIR) spectroscopic observations of the Seyfert 1.9 galaxy NGC 2992, obtained with the Gemini North Telescope and the Gran Telescopio CANARIAS (GTC). The *N*-band image reveals faint extended emission out to ∼3 kpc, and the polycyclic aromatic hydrocarbon features detected in the GTC/CanariCam 7.5–13 μm spectrum indicate that the bulk of this extended emission is dust heated by star formation. We also report arcsecond resolution MIR and far-IR imaging of the interacting system Arp 245, taken with the *Spitzer Space Telescope* and the *Herschel Space Observatory*. Using these data, we obtain nuclear fluxes using different methods and find that we can only recover the nuclear fluxes obtained from the subarcsecond data at 20–25 μm, where the active galactic nuclei (AGN) emission dominates. We fitted the nuclear IR spectral energy distribution of NGC 2992, including the GTC/CanariCam nuclear spectrum (∼50 pc), with clumpy torus models. We then used the best-fitting torus model to decompose the *Spitzer*/IRS 5–30 μm spectrum (∼630 pc) in AGN and starburst components, using different starburst templates. We find that, whereas at shorter MIR wavelengths the starburst component dominates (64 per cent at 6 μm), the AGN component reaches 90 per cent at 20 μm. We finally obtained dust masses, temperatures and star formation rates for the different components of the Arp 245 system and find similar values for NGC 2992 and NGC 2993. These measurements are within those reported for other interacting systems in the first stages of the interaction.

Key words: galaxies: active – galaxies: groups: individual: Arp 245 – galaxies: individual: NGC 2992 – galaxies: individual: NGC 2993 – galaxies: nuclei – infrared: galaxies.

1 INTRODUCTION

Active galactic nuclei (AGN) are powered by supermassive black holes, which release enormous quantities of energy in the form

---

★E-mail: igarcia@iac.es
†Marie Curie Fellow.

Published by Oxford University Press on behalf of the Royal Astronomical Society

of radiation or mechanical outflows to the host galaxy interstellar medium. This feedback is fundamental to the formation and evolution of the host galaxies (Hopkins & Quataert 2010). On the other hand, galaxy mergers and interactions or secular processes can generate gas inflows to the nuclear regions of galaxies, potentially triggering both AGN and central starbursts (SB; Hopkins et al. 2008). It has been proposed that the triggering mechanisms might depend on AGN luminosity (e.g. Ramos Almeida et al. 2012; Treister et al. 2012), with high-luminosity AGN (e.g. quasars and powerful radio galaxies) being more commonly triggered by galaxy interactions and low-to-intermediate luminosity AGN (e.g. Seyferts and low-ionization nuclear emission-line regions) by disc instabilities, galaxy bars, etc. However, this dependence is not univocal, and examples of both low-luminosity AGN in interacting systems and quasars in isolated and morphologically undisturbed galaxy hosts are also found in different galaxy samples (Lípari et al. 2004; Serra et al. 2006; Bessiere et al. 2012).

Seyfert galaxies are intermediate-luminosity AGN, characterized by a very bright unresolved nucleus generally hosted by a spiral galaxy (Adams 1977). They can be classified as type 1 or type 2 depending on orientation, according to the unified model (Antonucci 1993). This scheme proposes that there is dust surrounding the active nucleus distributed in a toroidal geometry, which obscures the central engines of type 2 Seyferts, and allows a direct view in the case of type 1. The dusty torus absorbs the intrinsic AGN radiation and, then, reprocesses it to emerge in the infrared (IR), peaking in the mid-IR (MIR; ∼5–30 μm).

MIR observations of the nuclear regions of active galaxies allow us to study the emission of dust heated by the AGN, but also by star formation (SF) when present (e.g. Radomski et al. 2003; Packham et al. 2005; Alonso-Herrero et al. 2014; Esquej et al. 2014). Prominent features in the MIR spectrum of Seyfert galaxies are the 9.7 μm silicate band and the polycyclic aromatic hydrocarbon (PAH) emission bands, although the latter can be diluted by the bright AGN continuum, and therefore they have lower equivalent widths (EWs) than those of non-active star-forming galaxies (see e.g. Alonso-Herrero et al. 2014; Ramos Almeida et al. 2014). The high angular resolution is crucial to correctly separating the nuclear emission from the foreground galaxy emission, as the MIR-emitting torus is very small ($r < 10$ pc; see e.g. Tristram et al. 2009; Burtscher et al. 2013).

To contribute to the understanding of the relation between nuclear activity, SF, torus properties and circumnuclear emission, here we use IR and optical imaging and MIR spectroscopy of the Seyfert galaxy NGC 2992. This inclined spiral galaxy ($b/a = 0.31$; de Vaucouleurs et al. 1991) is located at a luminosity distance of 36.6 Mpc and it is part of the interacting system Arp 245. This system is formed by NGC 2992, the spiral star-forming galaxy NGC 2993 (Usui, Saito & Tomita 1998) and the tidal dwarf galaxy Arp 245 North (hereafter Arp 245N; Duc et al. 2000). Two bright tidal features connect these three galaxies, suggesting that the system is in an early stage of the interaction (Duc et al. 2000). We selected the Arp 245 system for this IR study, and the galaxy NGC 2992 in particular, because of the plethora of multiwavelength data available in the literature, and because we have new far-IR (FIR) observations from the *Herschel Space Observatory* as well MIR data from CanariCam (CC) on the 10.4 m Gran Telescopio CANARIAS (GTC). NGC 2992 was observed with these telescopes because previous MIR imaging data revealed extended emission on nuclear scales, possibly related to the interaction with the other galaxies in the Arp 245 system. Our aim is to study the origin of this IR extended emission by combining the existing and the new IR observations. See Section 2 for a detailed description of the observations employed here.

NGC 2992 is classified as a Seyfert 1.9 in the optical, although it has changed its type between Seyfert 1.5 and 2 in the past (Trippe et al. 2008). It also exhibited huge variations in the X-rays (factor of ∼20; Gilli et al. 2000) and in the IR as well (Glass 1997). The IR variations were probably caused by a retriggered AGN and by different stages of the rebuilding of the accretion disc, with the disc rebuilding estimated to range between 1 and 5 years (Gilli et al. 2000). Besides, Glass (1997) found flux variability in the near-IR (NIR), and reported a fading of the source from 1978 to 1996, apart from a strong outburst in 1988. The galaxy shows a thick dust line at PA $\sim$ 25–30°, measured from north to east, which has been shown to be affecting the emission line profiles in the optical (Colina et al. 1987).

NGC 2992 also has evidence for intense SF (Quillen et al. 1999), with large-scale outflows observed in Hα, [O III]λ5007 Å and soft X-rays, driven either by jets or by an SB (Colina et al. 1987; Colbert et al. 1998). In fact, the molecular gas emission in NGC 2992 could be excited by processes associated with local SF (Quillen et al. 1999). The outflow component is distributed in two wide cones (Colina et al. 1987; Durret & Bergeron 1987; Colbert et al. 1996; Allen et al. 1999; Veilleux, Shopbell & Miller 2001), with the geometry of the biconical outflow being such that the southeastern cone is in front of the galaxy disc and the base of the northwestern outflow is behind it. Apart from the two main kinematic components of the ionized gas (rotation+outflow), an additional component is required to explain the departure of the ionized gas from the gravitational motion defined from the stars. This component would be related to the AGN, and not to the interaction (García-Lorenzo, Arribas & Mediavilla 2001). The hidden Seyfert nucleus is probably located at the apex outflow origin and at the centre of the bulge, but it does not seem to coincide with the kinematic centre of the disc (García-Lorenzo, Arribas & Mediavilla 2001).

Although NGC 2992 has been observed at several wavelengths, up to date there is not any detailed high-resolution IR analysis of this active galaxy or of the entire system. Here, we present a complete IR study of the interacting system Arp 245, focusing on NGC 2992. Section 2 describes the observations and data reduction. The main results, including a compilation of IR fluxes, are presented in Section 3. We explore different methods to recover the nuclear emission from low angular resolution data in Section 4. We derive relevant physical parameters of the dust emission in Section 5. Finally, in Section 6 we present the discussion and in Section 7 we summarize the main conclusions of this work.

Throughout this paper, we assumed a cosmology with $H_0 = 73$ km s^{-1} Mpc^{-1}, $\Omega_m = 0.27$, and $\Omega_\Lambda = 0.73$ for the Arp 245 system. This cosmology provides a luminosity distance of 36.6 Mpc and a spatial scale of 174 pc arcsec^{-1} (from the NASA/IPAC Extragalactic Database; NED).

2 OBSERVATIONS

In this section, we describe all the observations analysed in this work, which we divide in subarcsecond and arcsecond resolution data. Subarcsecond data are from 8–10 m-class ground-based telescopes and from the *Hubble Space Telescope* (*HST*), which allow us to resolve the innermost regions of the galaxies. Arcsecond resolution data correspond to observations taken with the *Spitzer Space Telescope* and the *Herschel Space Observatory*, which have lower spatial resolution but higher sensitivity. Details of the observations are summarized in Table 1.

Table 1. Summary of the imaging and spectroscopic observations. The σ corresponds to the standard deviation of the sky background in mJy pixel^{-1} units. Note that the PACS observations were done using the normal/cross scan pattern, whereas the small map SPIRE observations were done using the nominal/cross scan pattern.

Wavelength $\lambda_c/\Delta\lambda$ (μm)	Imaging Filter/ Band	Telescope/Instrument Imaging	Spatial resolution (arcsec)	(pc)	Pixel scale (arcsec pixel^{-1})	Standard deviation σ (10^{-2})	Date (UT)
0.6/0.15	*F606W*	*HST*/WFPC2	0.095	17	0.046	1.3	1994 Oct 18
2.07/0.6	*F205W*	*HST*/NICMOS2	0.107	19	0.075	12.9	1998 Oct 15
3.6/0.75	Ch1	*Spitzer*/IRAC	1.85	322	0.6	0.01	2004 Dec 21
4.5/1.02	Ch2	*Spitzer*/IRAC	1.77	308	0.6	0.01	2004 Dec 21
5.8/1.43	Ch3	*Spitzer*/IRAC	2.15	374	0.6	0.08	2004 Dec 21
8/2.91	Ch4	*Spitzer*/IRAC	2.79	485	0.6	0.05	2004 Dec 21
11.2/2.4	N’	GEMINI/MICHELLE	0.32	56	0.1005	7.6	2006 May 12
18.1/1.9	Qa	GEMINI/MICHELLE	0.53	92	0.1005	68.4	2006 May 12
24/4.7	Ch1	*Spitzer*/MIPS	6.06	1054	1.225	0.2	2008 Jun 23
70/10.6	Blue	*Herschel*/PACS	5.25	914	1.4	8.9	2011 May 16
100/17	Green	*Herschel*/PACS	6.75	1175	1.7	12.3	2011 May 16
160/30.2	Red	*Herschel*/PACS	10.80	1879	2.85	13.1	2011 May 16
250/75.76	PSW	*Herschel*/SPIRE	17.63	3068	6	48.3	2010 Jun 21
350/102.94	PMW	*Herschel*/SPIRE	24.49	4261	10	94.3	2010 Jun 21
500/200	PLW	*Herschel*/SPIRE	34.66	6031	14	52.4	2010 Jun 21

Wavelength (μm)	Spectroscopy Slit width (arcsec)	Telescope/Instrument Spectroscopy	Spectral resolution $\lambda/\Delta\lambda$	Pixel scale (arcsec pixel^{-1})	Exposure time (s)	Date (UT)
7.5–13	0.52	GTC/CANARICAM	~175	0.0798	943	2014 Feb 13
8–13	0.4	GEMINI/MICHELLE	~200	0.183	1200	2007 Mar 25
5.2–14.5	3.6–3.7	*Spitzer*/IRS SL	60–127	1.8	14	2005 Dec 10
14–38	10.5–10.7	*Spitzer*/IRS LL	57–126	5.1	6	2005 Dec 10

2.1 Subarcsecond resolution data

2.1.1 *MIR Gemini/MICHELLE observations*

Two images were taken in the N' (λ_c = 11.2 μm) and Qa (λ_c = 18.1 μm) filters using the instrument MICHELLE (Glasse, Atad-Ettedgui & Harris 1997) on the 8.1 m Gemini-North Telescope. MICHELLE is an MIR (7–26 μm) imager and spectrograph, which uses a Si:As detector, covering a field of view (FOV) of 32 arcsec ×24 arcsec on the sky. Its pixel scale is 0.1005 arcsec. The standard MIR chopping–nodding technique was used to remove the time-variable sky background and the thermal emission from the telescope. The chopping and nodding throws were 15 arcsec, optimal for the galaxy size (minor axis~2 arcsec) and perpendicular to the semimajor axis of the galaxy.[1] The on-source integration times were 150 s for both galaxy images. Besides, images of a point spread function (PSF) standard star were obtained immediately after the science target in the N' and Qa filters for accurately sampling the image quality, and to allow flux calibration. We measured angular resolutions of 0.32 arcsec and 0.53 arcsec from the full width at half-maximun (FWHM) of these PSF standard stars. The fully reduced images of NGC 2992, taken from Ramos Almeida et al. (2009), are presented in Fig. 1. The N-band image shows a morphology consisting of a dominant point source and faint extended emission along PA ~ 30°, whereas the Q-band image shows unresolved emission only. See Section 3.2 for more details.

In addition, an MIR spectrum covering the spectral range 8–13 μm was obtained with the low resolution ($R = \lambda/\Delta\lambda \sim 200$) MICHELLE N-band grating. A slit of ~0.4 arcsec width was used, oriented at PA = 0°, and the on-source integration time was 1200 s. We used the reduced and flux calibrated spectrum from Colling (2011), also presented in Esquej et al. (2014).

2.1.2 *MIR Gran Telescopio CANARIAS/CanariCam observations*

We obtained an N-band spectrum (7.5–13 μm) of NGC 2992, using the low spectral resolution ($R \sim 175$) grating available in the instrument CC (Telesco et al. 2003), on the 10.4 m GTC. CC is an MIR (7.5–25 μm) imager with spectroscopic, coronagraphic and polarimetric capabilities and uses a Si:As detector, which covers an FOV of 26 arcsec × 19 arcsec on the sky and it has a pixel scale of 0.0798 arcsec (hereafter 0.08 arcsec). The slit, of width ~0.52 arcsec, was oriented at PA = 30°, following the faint extended emission revealed by the Gemini/MICHELLE imaging data (see Fig. 1). The total on-source integration time was 943 s and the standard MIR chopping–nodding technique was used, with chop and nod throws of 15 arcsec.

The data were taken as part of an ESO/GTC large programme (182.B-2005; PI: Alonso-Herrero), aimed to conduct an MIR survey of nearby AGN by exploiting the unique capabilities of CC on the GTC (see Alonso-Herrero et al. 2013, 2014 for further details). The data reduction was carried out with the *RedCan* pipeline (González-Martín et al. 2013), which performs sky subtraction, stacking of individual observations, rejection of bad frames, wavelength calibration, trace determination and spectral extraction. We extracted a nuclear spectrum as a point source, and another spectrum as an extended source in an aperture radius of 5.2 arcsec (~905 pc), which we then use to characterize the extended emission (see

---

[1] The chopping throw was chosen according to the galaxy size in the Gemini/MICHELLE image. We note that both the resolution and sensitivity of the *Spitzer Space Telescope* and Gemini are completely different, and thus, the large-scale IR emission that we detect in the *Spitzer* images is completely absent in the ground-based image and it does not affect the latter.

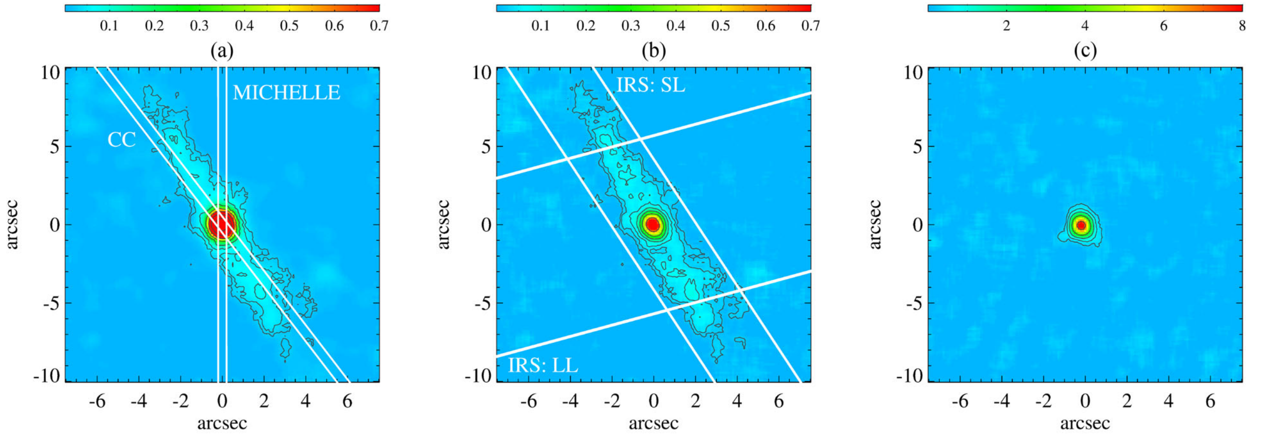

Figure 1. Gemini/MICHELLE images of NGC 2992. (a) MICHELLE 11.2 μm image with the CC and MICHELLE slits overlaid. (b) PSF-subtracted MICHELLE 11.2 μm image with the *Spitzer*/IRS slits overlaid (see Section 2.2.1). (c) MICHELLE 18.1 μm image. All images are smoothed (box of 6 pixels) and have their own contours overlaid (in black). Colour bars correspond to fluxes in mJy units. North is up, and east to the left.

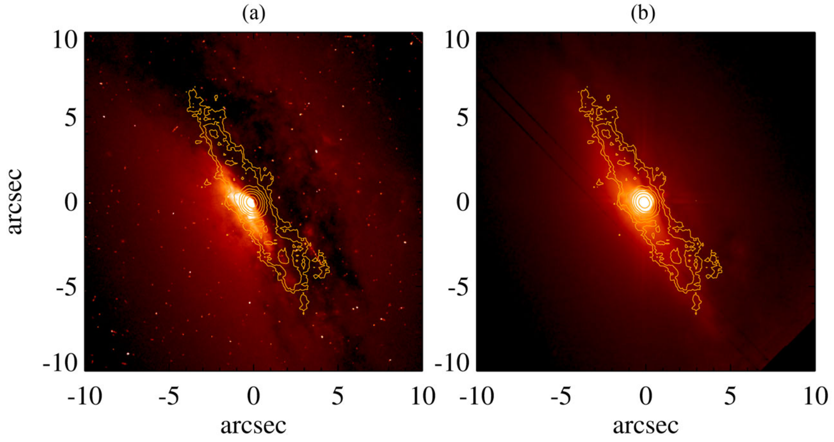

Figure 2. *HST*/WFPC2 optical image of NGC 2992 in the *F*606*W* filter (left-hand panel), and *HST*/NICMOS NIR image in the *F*205*W* filter (right-hand panel). Orange contours correspond to the PSF-subtracted Gemini/MICHELLE 11.2 μm image (panel b in Fig. 1). North is up, and east to the left.

Section 3.1.2). Note that in the case of point source extraction, *RedCan* uses an aperture that increases with wavelength to take into account the decreasing angular resolution, and it also performs a correction to account for slit losses. For the extended source extraction, a fixed 5.2 arcsec aperture and no slit-loss corrections were applied (see González-Martín et al. 2013 for further details on CC data reduction).

2.1.3 *Optical and NIR HST observations*

We downloaded the fully reduced optical and NIR imaging data of NGC 2992 from the ESA Hubble Legacy Archive.[2] The optical image, shown in the left-hand panel of Fig. 2, was observed with the *F*606*W* filter ($\lambda_c = 5975$ Å) using the Wide Field Planetary Camera 2 (WFPC2), which has an FOV of 2.7 arcmin ×2.7 arcmin on the sky and a pixel scale of 0.046 arcmin. The NIR image (see right-hand panel of Fig. 2) was observed with the *F*205*W* filter ($\lambda_c = 2.07$ μm) using the Near-Infrared Camera and Multi-Object Spectrometer (NICMOS), which has an FOV of 19.2 arcmin × 19.2 arcmin on the sky and a pixel scale of 0.075 arcmin (NIC2 camera). The downloaded NICMOS and WFPC2 images were reduced using the NICRED package (McLeod 1997) and the Space Telescope Science Analysis System (STSDAS) within IRAF.[3]

The optical and NIR data were taken as part of the Hubble programmes P5479 (cycle:4, PI: M. Malkan) and P7869 (cycle:7, PI: A. Quillen), respectively. We refer the reader to Malkan, Gorjian & Tam (1998) and Quillen et al. (1999) for further details on these *HST* observations.

2.2 Arcsecond resolution data

2.2.1 *MIR Spitzer Space Telescope observations*

We downloaded imaging data of the Arp 245 system from the Spitzer Heritage Archive, taken with the instruments Infrared Array Camera (IRAC; Fazio et al. 2004) and Multiband Imaging Photometer for *Spitzer* (MIPS; Rieke et al. 2004). The IRAC FOV is 5.2 arcmin × 5.2 arcmin on the sky and its pixel scale is 1.2 arcsec,

---

[2] http://archives.esac.esa.int/hst/

[3] IRAF is distributed by the National Optical Astronomy Observatory, which is operated by the Association of Universities for Research in Astronomy (AURA) under cooperative agreement with the National Science Foundation.

whereas the MIPS FOV is 5.4 arcmin × 5.4 arcmin on the sky and its pixel scale is 2.45 arcsec.

In addition, a low-resolution MIR spectrum of NGC 2992 was retrieved from the Cornell Atlas of *Spitzer*/IRS Source (CASSIS v4; Lebouteiller et al. 2011). The spectrum was obtained using the InfraRed Spectrograph (IRS; Houck et al. 2004). The observation was made in staring mode using the two low-resolution ($R \sim 60$–120) IRS modules: the short-low (SL; 5.2–14.5 μm) and the long-low (LL; 14–38 μm). The slits were oriented as shown in Fig. 1 and their widths are 3.6 arcsec and 10.5 arcsec for the SL and LL modules, respectively.

The IRAC imaging data (3.6, 4.5, 5.8 and 8.0 μm) and the IRS spectrum were taken as part of the *Spitzer* programme P96 (PI: J. R. Houck), and the MIPS imaging data (24 μm) under program P40936 (PI: G. Rieke). In the case of the IRAC images, we just downloaded the mosaicked data from the *Spitzer* archive, which have a pixel scale of 0.6 arcsec. On the other hand, the MIPS image was reprocessed using the MOsaicking and Point source EXtraction (MOPEX) software. Background gradients were removed by self-calibrating the data (see section 8.1 of the MIPS Instrument Handbook 2011 for details) and the resulting mosaics were resampled to a pixel size of 1.225 arcsec.

We downloaded the IRS spectrum from the CASSIS data base. The spectrum was reduced with the CASSIS software, using the optimal extraction to get the best signal-to-noise (S/N) ratio. We only needed to apply a small offset to stitch together the different modules, taking the shorter wavelength module (SL2; 5.2–7.6 μm) as the basis, which has associated a slit width of 3.6 arcsec (∼630 pc). The IRS spectrum is shown in left-hand panel of Fig. 3 (black dashed line) and it was also presented in Esquej et al. (2014).

2.2.2 *FIR Herschel Space Observatory observations*

FIR imaging data of the Arp 245 system were obtained with the Photodetector Array Camera and Spectrometer (PACS; Poglitsch et al. 2010) and the Spectral and Photometric Imaging REceiver (SPIRE; Griffin et al. 2010) on-board of the *Herschel Space Observatory* (Pilbratt et al. 2010). The data are part of the guaranteed time proposal 'Herschel imaging photometry of nearby Seyferts galaxies: testing the coexistence of AGN and SB activity and the nature of the dusty torus' (PI: M. Sánchez-Portal).

The PACS instrument has an FOV of 1.75 arcmin × 3.5 arcmin on the sky and three different bands (70, 100 and 160 μm), with beam sizes of 5.6, 6.8 and 11.3 arcsec FWHM, respectively. The PACS observations were carried out using the mini-map mode, consisting of two concatenated 3 arcmin scan line maps, at 70° and 110° (in array coordinates). This results in a map with a highly homogeneous exposure within the central 1 arcmin area. The SPIRE instrument has an FOV of 4 arcmin × 8 arcmin on the sky and three different bands (250, 350 and 500 μm), whose beam sizes are 18.1, 25.2 and 36.9 arcsec FWHM, respectively. These three available bands were observed simultaneously using the small map mode, whose area for scientific use is around 5 arcmin × 5 arcmin.

The PACS data processing was carried out by means of two tools: the Herschel Interactive Processing Environment (HIPE; Ott 2010) and SCANAMORPHOS (Roussel 2012). In order to build the Level 1 products, we used HIPE v8.0.1 with the PACS calibration data base V32. This Level 1 processing included detecting and flagging bad pixels, converting the analogue to digital units readings to flux units (Jy pixel^{-1}) and adding the pointing information. We did not attempt to perform deglitching at this stage to prevent the bright AGN nucleus to be affected by the multiresolution median transform deglitching process. The final maps were built from the Level 1 products using SCANAMORPHOS v15, which performs a baseline subtraction, correction of the striping effect due to the scan process, removal of global and individual pixel drifts, and finally the map assembly using all the nominal and cross-direction scans.

For the SPIRE data processing, we built the Level 1 products with HIPE v8.0.1 and the SPIRE calibration data base v8.1. The Level 1 processing included detection of thermistor jumps in the time line, frame deglitching, low-pass filter correction, conversion of readings to flux units (Jy beam^{-1}), temperature drift and bolometric time response corrections, and addition of pointing information. The final maps were built from the Level 1 using the Naïve Mapper functionality integrated in HIPE v8.0.1. This mapping strategy simply projects the integrated power seen by each bolometer on to the nearest sky map pixel. Once all the detector signals have been mapped, the flux density map and the standard deviations are calculated.

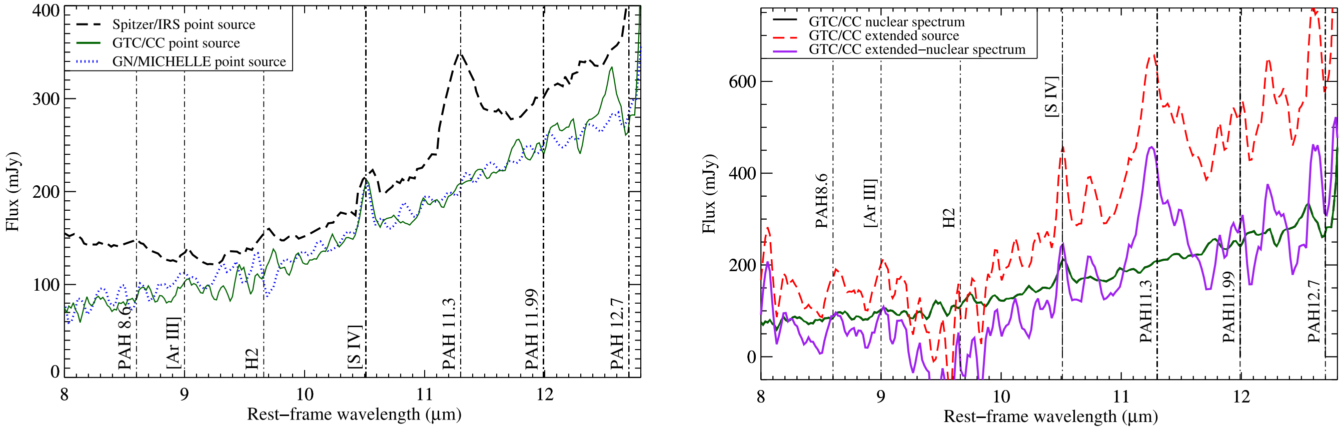

Figure 3. Left-hand panel: *Spitzer*/IRS rest-frame spectrum (∼630 pc) of NGC 2992 (dashed black line) and GTC/CC and Gemini/MICHELLE rest-frame nuclear spectra (∼47 and ∼66 pc) of NGC 2992 (solid green and dotted blue lines, respectively), extracted as a point source. Right-hand panel: GTC/CC spectrum of NGC 2992 extracted as an extended source in an aperture radius of 5.2 arcsec ∼905 pc (dashed red line), GTC/CC nuclear spectrum (as in left-hand panel; solid green line) and spectrum of the extended emission (solid purple line), obtained by subtracting the nuclear spectrum from the one extracted in the 5.2 arcsec aperture radius. In both panels, the vertical dotted lines indicate the position of typical star-forming regions/AGN emission lines/bands. All spectra have been smoothed (2 pixel box).

3 IR EMISSION OF THE SYSTEM

3.1 Nuclear region of NGC 2992

In this section, we study in detail the properties of the inner 100 pc of the galaxy NGC 2992 as well as the surrounding faint extended emission.

3.1.1 Imaging

In Fig. 1, we show the high angular resolution MIR Gemini/MICHELLE images of NGC 2992. The 11.2 μm image reveals faint emission along PA ∼ 30° and extending out to ∼3 kpc (see more details in Section 3.2.1). This emission is coincident with the extended emission shown in the NIR *HST* image (right-hand panel of Fig. 2). On the other hand, the optical *HST* image shows a thick dust lane that partly obscures the nucleus and whose orientation coincides with that of the extended emission (30°; left-hand panel of Fig. 2). For the image registration, we first used the galaxy nucleus in the MICHELLE and NICMOS images, and then we used different stars in the FOV that the NICMOS and WFPC2 images have in common for centring the optical image. We note that the galaxy nucleus in the *HST*/NICMOS image is saturated. Finally, we measured a surface brightness of 4.84 ± 0.07 mJy arcsec^{-2} for the extended emission in the 11.2 μm image with the PHOT task of IRAF. We used an aperture of 1 arcsec diameter in two different positions at both sides of the nucleus and we averaged the two measurements.

In addition to the extended emission seen in the 11.2 μm image there is an unresolved nuclear component, which is also present in the *Q*-band image. Ramos Almeida et al. (2009) estimated MIR nuclear fluxes of 175 and 521 mJy in the *N* and *Q* bands, respectively, by subtracting the PSF standard stars, observed in each filter before or after the science observations, from the galaxy profiles. In the central panel of Fig. 1, we show the PSF-subtracted *N*-band image of the galaxy, with the PSF scaled at 90 per cent.

3.1.2 Spectroscopy

In the left-hand panel of Fig. 3, we show the GTC/CC and Gemini/MICHELLE 8–13 μm nuclear spectra of NGC 2992, both extracted as a point source. The GTC/CC spectrum has a spatial resolution of 0.27 arcsec and the Gemini/MICHELLE spectrum of 0.38 arcsec, which correspond to physical scales of ∼47 pc and ∼66 pc, respectively. Both angular resolutions were determined from the FWHM of the PSF star acquisition images.

Despite the different slit orientations (see Fig. 1) and the time difference between the observations (∼7 yr), both spectra are practically identical. In spite of the IR variability reported by Glass (1997), we do not see any difference either in flux or shape. These spectra do not show PAH features and they exhibit [S IV]λ10.5 μm emission, which can originate in the narrow-line region (NLR) and it is usually considered an AGN tracer (Dasyra et al. 2011). However, this emission line can also be produced in star-forming regions, as shown by Pereira-Santaella et al. (2010), due to its relatively low ionization potential (35 eV). For comparison, in the left-hand panel of Fig. 3 we show the *Spitzer*/IRS spectrum in the same spectral range as the GTC/CC and Gemini/MICHELLE spectra, which has a spatial resolution of 3.6 arcsec, that corresponds to a physical scale of ∼630 pc. Unlike the nuclear spectra, the IRS spectrum shows 8.6 and 11.3 μm PAH bands, indicative of the presence of SF on the scales probed by *Spitzer*.

In the right-hand panel of Fig. 3, we show the nuclear GTC/CC spectrum, extracted as an extended source in an aperture radius of 5.2 arcsec (∼905 pc), the GTC/CC nuclear spectrum extracted as point source and the spectrum of the extended emission. The latter was obtained by subtracting the nuclear spectrum from the one extracted in the large aperture, in order to get rid of the AGN contribution. We chose this large aperture to increase the S/N of the extended emission spectrum. The spectra of the extended emission, before and after subtracting the AGN contribution, clearly show 11.3 μm PAH feature and the [S IV]λ10.5 μm emission line, exactly as the *Spitzer*/IRS spectrum on scales of ∼630 pc. Thus, the faint extended emission that we detect in the Gemini/MICHELLE *N*-band image of the galaxy is, as least in part, due to SF. On the other hand, if we compare these spectra with the GTC/CC and Gemini/MICHELLE nuclear spectra shown in the left-hand panel of Fig. 3, we can conclude that either the PAH features have been destroyed in the inner ∼50 pc of NGC 2992, or are diluted by the strong AGN contiuum (see Alonso-Herrero et al. 2014 and Ramos Almeida et al. 2014).

3.1.3 Nuclear SED modelling with clumpy torus models

Recent studies assumed a clumpy distribution of dust surrounding AGN to explain the properties of the nuclear IR spectral energy distribution (SED) of Seyfert galaxies (Mason et al. 2006, 2009; Nikutta, Elitzur & Lacy 2009; Ramos Almeida et al. 2009, 2011a,c, 2014; Hönig & Kishimoto 2010; Alonso-Herrero et al. 2011, 2012a, 2013; Lira et al. 2013). Here, we used the Nenkova et al. (2008a,b) clumpy torus models, commonly known as CLUMPY, and the Bayesian tool *BayesClumpy* (Asensio Ramos & Ramos Almeida 2009, 2013) to fit the nuclear IR emission of NCG 2992. The CLUMPY models are defined by six parameters (see Table 2), in addition to the foreground extinction and the vertical shift required to match the model to the observed SED. A detailed description of the Bayesian inference applied to the CLUMPY models can be found in Asensio Ramos & Ramos Almeida (2009).

Table 2. Clumpy model parameters, intervals considered as uniform priors, median and MAP values of the posteriors resulting from the fit of NGC 2992 nuclear SED. (σ: width of clouds angular distribution; Y: radial extent of the torus; N_0: clouds along equatorial ray; q: index of the radial density profile; i: inclination angle of the torus (Note: $i = 0°$ is face-on and $i = 90°$ is edge-on); τ_V: optical depth per single cloud; $A_V^{(\mathrm{for})}$: foreground extinction). The last four rows correspond to the torus outer radius, the AGN bolometric luminosity, the torus gas mass and the hydrogen column density derived from the fit.

Parameter	Prior	Median	MAP
σ	[15°, 35°]	$34°\pm1°$	35°
Y	[5, 100]	$16\pm^{3}_{4}$	12
N_0	[1, 15]	14 ± 1	15
q	[0, 3]	$0.6\pm^{0.3}_{0.5}$	0.5
i	[45°, 65°]	$64°\pm1°$	65°
τ_V	[5, 150]	$105\pm^{12}_{15}$	109
$A_V^{(\mathrm{for})}$	[2, 5] mag	$4.1\pm^{0.9}_{0.5}$ mag	5.0 mag
R_o	–	$1.4\pm^{0.5}_{0.4}$ pc	1.2 pc
$\mathrm{L}_{\mathrm{bol}}^{\mathrm{AGN}}/10^{43}$	–	$5.9\pm^{1.2}_{0.9}$ erg s^{-1}	5.8 erg s^{-1}
$M_{\mathrm{torus}}/10^5$	–	$1.3\pm^{0.3}_{0.2}$ $\mathrm{M}_\odot$	0.9 $\mathrm{M}_\odot$
$N_{\mathrm{H}}/10^{24}$	–	1.7 ± 0.2 cm^{-2}	3.4 cm^{-2}

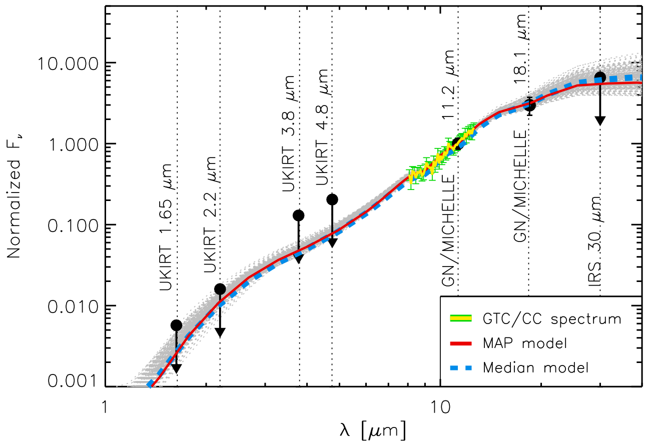

Figure 4. Nuclear IR SED of NGC 2992 normalized at 11.2 μm (thick yellow line: GTC/CC nuclear spectrum; black dots: UKIRT NIR fluxes from Alonso-Herrero et al. (2001) and Gemini/MICHELLE 11.2, 18.1 μm fluxes from Ramos Almeida et al. (2009) and 30 μm flux from the *Spitzer*/IRS spectrum). Solid red and dashed blue lines correspond to the MAP and median models, respectively. Grey curves are the clumpy models sampled from the posterior and compatible with the data at 1σ level.

We constructed the nuclear IR SED of NGC 2992 using the GTC/CC spectrum, which is more recent and has better angular resolution than the Gemini/MICHELLE one, extracted as a point source and resampled to 50 points; the UKIRT NIR nuclear fluxes from Alonso-Herrero et al. (2001); the MICHELLE MIR fluxes from Ramos Almeida et al. (2009); and the 30 μm flux from the *Spitzer*/IRS spectrum (see Fig. 4). There is good agreement between the flux calibration of the nuclear spectrum and the nuclear 11.2 μm flux, as we only measured a 10 per cent mismatch between them. For consistency, we scaled the spectrum to the nuclear 11.2 μm flux and we estimated a 15 per cent total uncertainty for the GTC/CC spectrum by quadratically adding the errors in the flux calibration and point source extraction. We used the NIR nuclear photometry as upper limits because of the lower angular resolution of the UKIRT data. We did not use the *HST*/NICMOS image available in the archive for obtaining an NIR nuclear flux because the galaxy nucleus is saturated. We finally considered the IRS 30 μm flux as an upper limit, due to the low angular resolution of *Spitzer*.

We fitted the SED of NGC 2992 considering reprocessed torus emission and foreground extinction, using the IR extinction curve of Chiar & Tielens (2006). We used the prior $A_V^{\rm (for)}$ = [2,5] mag in our fit, taking into account the extinction value of $A_V \sim 4$ mag reported by Chapman et al. (2000) for the innermost region of the galaxy. The opening angle of the ionization cones is 130°, as measured from the [O III] image reported by García-Lorenzo, Arribas & Mediavilla (2001). This would correspond to a torus width of 25° and therefore we used the prior σ = [15°, 35°] in our fit. We also used the prior i = [45°, 65°] for the inclination angle of the torus, based on the values reported for the orientation of the accretion disc by Gilli et al. (2000) using X-ray data, and from modelling of the kinematics of the NLR presented in Müller-Sánchez et al. (2011). The result of the fitting process are the posterior distributions of the parameters, but we can also translate the results into a best-fitting model, described by the combination of parameters that maximizes the posterior (maximum-a-posteriori; MAP) and a median model, computed with the median value of each posterior (see Fig. 4). The MAP and median parameters of NGC 2992 are shown in Table 2.

Table 3. NGC 2992 bolometric luminosities obtained from the 2–10 keV X-ray intrinsic luminosities (by multiplying by a factor 20 as in Elvis et al. 1994). For the non-intrinsic X-ray luminosity values, a factor of 70 has been used in addition to the bolometric correction factor, as in Marinucci et al. (2012).

$L_{\rm bol}^{\rm X-ray}$ (erg s^{-1})	Date	Telescope	Reference
2.3× 10^{44}	1978	*HEAO 1*	Mushotzky (1982)
8.9× 10^{43}	1979	*Einstein*	Turner et al. (1991)
2.5× 10^{43}	1990	*Ginga*	Nandra & Pounds (1994)
1.4× 10^{43}	1994	*ASCA*	Weaver et al. (1996)
1.2× 10^{43}	1997	*BeppoSAX 1*	Gilli et al. (2000)
1.4× 10^{44}	1998	*BeppoSAX 2*	Gilli et al. (2000)
2.6× 10^{44}	2003	*XMM–Newton*	Shu et al. (2010)
2.5× 10^{44}	2003	*XMM–Newton*	Brightman & Nandra (2011)
3.2× 10^{43}	2005	*Suzaku*	Yaqoob et al. (2007)

From the fit presented in Fig. 4 we find that we require a foreground extinction, unrelated to the torus, of $A_V^{\rm (for)} \sim 5$ mag in the case of the MAP model. This is in good agreement with the value derived from the fit of the silicate feature reported by Colling (2011) using the Gemini/MICHELLE nuclear spectrum of NGC 2992 ($\tau_{9.7\,\mu{\rm m}} \sim 0.3$).

We derived a small torus radius from the MAP torus model, of 1.2 pc, in agreement with the results from interferometry of nearby Seyfert galaxies (see Burtscher et al. 2013 and references therein). The torus covering factor is ∼0.5, which is more similar to the values reported by Ramos Almeida et al. (2011c) for Seyfert 1 galaxies, and which could explain the variations in Seyfert type of NGC 2992 (see Section 6.1 for a discussion). We derived the AGN bolometric luminosity from the vertical shift applied to the MAP model to fit the data (see Ramos Almeida et al. 2011c and Alonso-Herrero et al. 2011 for further details), and we obtained $L_{\rm bol}^{\rm AGN} = 5.8 \times 10^{43}$ erg s^{-1}. This is consistent with the most recent X-ray observations available in the literature ($L_{\rm bol}^{\rm X-ray} = 3.2 \times 10^{43}$ erg s^{-1}; see Table 3), taken in 2005. Using the MAP value of the total optical extinction produced by the torus ($A_V^{\rm torus} = 1776$ mag), we can derive the column density using the dust-to-gas ratio $N_{\rm H}^{\rm LOS} = 1.9 \times 10^{21}$ x $A_V^{\rm torus}$ (Bohlin, Savage & Drake 1978). This gives $N_{\rm H} = 3.4 \times 10^{24}$ cm^{-2}, which is within the range reported by Weaver et al. (1996) for the cold dense gas detected in the inner ∼3 pc of the galaxy in the X-rays (∼10^{23}–10^{25} cm^{-2}). We also estimated the torus gas mass using equation 4 in Nenkova et al. (2008b), which is a function of the parameters σ, N_0, τ_V, Y and the sublimation radius of the torus. We obtain a torus gas mass of $M_{\rm torus} = 9 \times 10^4$ M$_\odot$, which is of the same order as that measured by García-Burillo et al. (2014) for the central 20 pc of the Seyfert 2 NGC 1068 using cycle 0 data from the Atacama Large Millimeter/submillimeter Array (ALMA; $M_{\rm gas} = 1.2 \times 10^5$ M$_\odot$). The good agreement between $L_{\rm bol}^{\rm X-ray}$ and $L_{\rm bol}^{\rm AGN}$, in addition to the good match between the models and the IR observations, confirm that the clumpy torus fitted here provides a realistic scenario for the inner parsecs of NGC 2992.

3.2 Large-scale emission

In this section, we study the large-scale IR morphology of the interacting system Arp 245 (see Fig. 5), which consists of three galaxies undergoing strong tidal interaction: the spirals NGC 2992 and NGC 2993 and the tidal dwarf galaxy Arp 245N. There is a fourth galaxy that is also part of the system: FGC 0938, but it lies outside the *Spitzer* and *Herschel* FOVs.

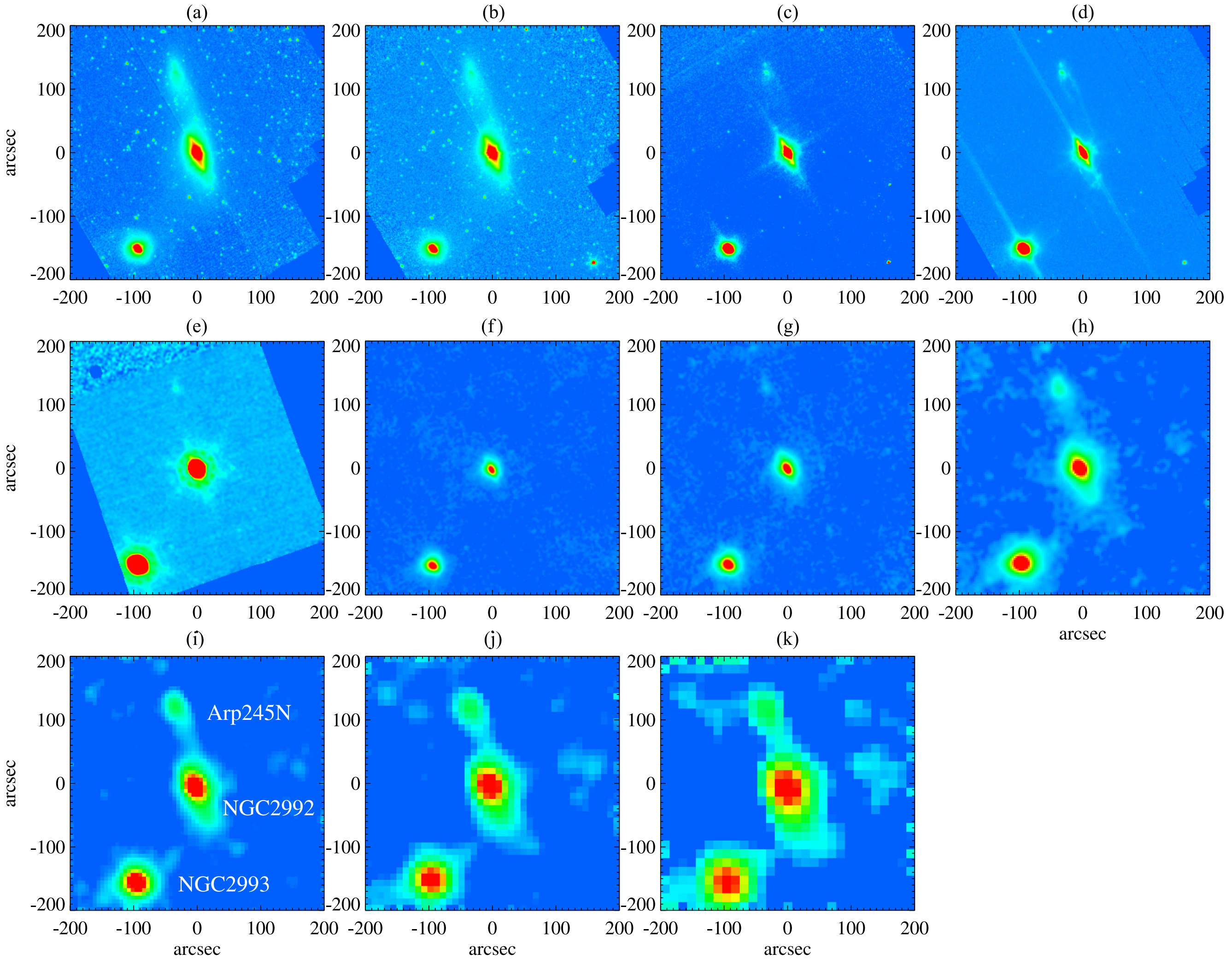

Figure 5. *Spitzer* and *Herschel* images of the Arp 245 system. NGC 2992 is the central galaxy, NGC 2993 is at the bottom-left corner of the images, and Arp 245N is at the top. The four IRAC channels (3.6, 4.5, 5.8 and 8 μm) are shown in panels (a)–(d), the MIPS channel 1 image (24 μm) in panel (e), the PACS 70, 100 and 160 μm images in panels (f)–(h), and the SPIRE 250, 350 and 500 μm images in panels (i)–(k). All images have been smoothed (3 pixels box). North is up, and east to left.

3.2.1 *NGC 2992*

In Fig. 6, we show *Spitzer*/IRAC and MIPS, and *Herschel*/PACS and SPIRE images of NGC 2992 in a 120 arcsec × 120 arcsec FOV. The extended emission in the IRAC images is elongated in the same direction as the faint extended emission detected in the Gemini/MICHELLE *N* band and *HST*/NICMOS images (see Fig. 2), and it also coincides with the orientation of the galaxy major axis. Considering that the spectrum of the extended emission shows a strong 11.3 μm PAH feature (see Section 3.1.2), the bulk of this faint emission is likely produced by dust heated by SF. In the case of the IRAC images the source of the IR emission depends on the band we look at, with the 3.6 and 4.5 μm emission likely dominated by starlight and the 5.8 and 8 μm emission by dust heated by SF and the AGN (e.g. Draine et al. 2007).

The MIPS 24 μm image, on the other hand, is rather point-like, as the Gemini/MICHELLE *Q*-band emission seen in the right-hand panel of Fig. 1. The 70 and 100 μm emission seen in the *Herschel*/PACS images (panels f and g in Fig. 6) is barely resolved and slightly elongated in the same direction as the *Spitzer*/IRAC images. From 160 to 500 μm, the intensity of the extended emission increases significantly, produced by cooler dust in the galaxy (panels h–k in Fig. 6).

3.2.2 *Arp 245 system*

In Fig. 5, we show *Spitzer*/IRAC and MIPS, and *Herschel*/PACS and SPIRE images of the interacting system Arp 245. NGC 2992 and Arp 245N show clearly distorted morphologies, and they are linked by a tidal tail which appears very bright in the *Spitzer*/IRAC images. The bridge (Arp 245 Bridge) between NGC 2992 and NGC 2993 is more conspicuous in the *Herschel*/SPIRE maps, indicating the presence of cooler dust.

We measured total galaxy fluxes for the three galaxies to construct their IR SEDs, which are shown in Fig. 7 and Table 4. We used a large aperture (60 arcsec radius for NGC 2992/93 and 25 arcsec radius for Arp 245N) to collect all the galaxy flux,[4] and subtracted

---

[4] In the case of the MIPS 24 μm image, we used an aperture radius of 25 arcsec to calculate the total flux of NGC 2993, which is too close to the image edge.

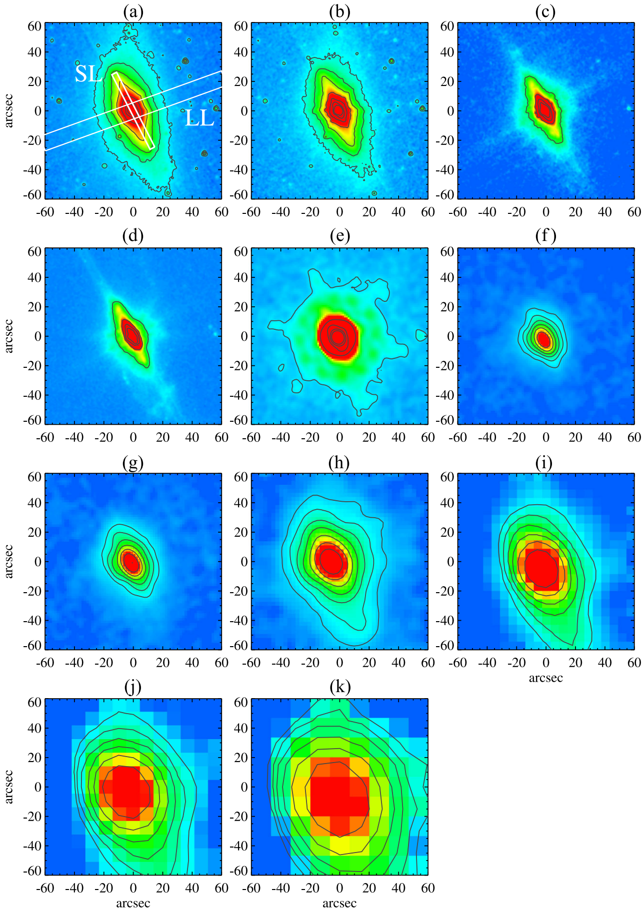

Figure 6. Same as in Fig. 5, but for NGC 2992. Panel (a) shows the orientation of the *Spitzer*/IRS slits. All images have been smoothed (3 pixels box) and have their own contours overlaid (in black).

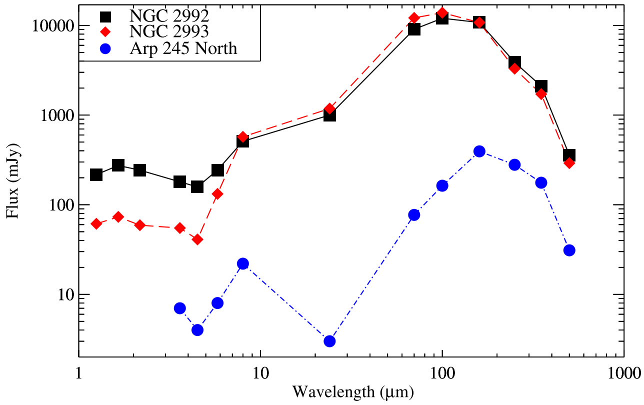

Figure 7. NGC 2992, NGC 2993 and Arp 245N total IR SEDs (black solid, red dashed and blue dot–dashed lines, respectively).

the sky background. The IR SEDs of NGC 2992/93 shown in Fig. 7 also include NIR total fluxes from 2MASS, reported by Jarrett et al. (2003).

As can be seen from Fig. 7, the total SEDs of NGC 2992 and NGC 2993 are very similar at wavelengths longer than 8 μm. This similarity is likely related to the presence of intense SF in both galaxies, which heats the dust at similar temperatures. This is corroborated by the SED fitting presented in Section 5. On the other hand, the total SEDs are different in flux level at shorter wavelengths ($\lambda < 8$ μm), with NGC 2992 being brighter. Considering that the 3.6 and 4.5 μm emission is dominated by the Rayleigh-Jeans tail of stellar photospheric emission (Howell et al. 2007), the brighter NIR SED of NGC 2992 is likely due to its larger stellar mass, as compared to that of NGC 2993 (Duc et al. 2000), and, to a lesser extent, to the extra-contribution from dust heated by the AGN. Nevertheless, we note that the SED shapes at these shorter wavelengths are very similar, and characteristic of old stellar populations.

The fainter SED of Arp 245N has a similar shape to those of NGC 2992 and NGC 2993 SEDs, except in the ∼24–100 μm range, where the fluxes are lower compared to other wavelengths. This can be indicative of a relatively weak illuminating radiation field that may possibly be consistent with weak SF activity (see Section 5). We refer the reader to Draine & Li (2007) and Dale et al. (2014) for further discussion.

4 RECOVERING NUCLEAR INFORMATION FROM ARCSECOND RESOLUTION DATA

In this section, we used different methods to try to recover the nuclear emission of NGC 2992 from the lower angular resolution data of *Spitzer* and *Herschel*. This kind of analysis is important due to the paucity of ground-based MIR instruments and to the difficulty of observing in the MIR range from ground. In this case, we have the opportunity to compare with the nuclear fluxes obtained from the high angular resolution data presented here, obtained using GTC/CC and Gemini/MICHELLE.

4.1 Recovering the nuclear IR SED

In order to try to recover the nuclear IR SED of NGC 2992 from low angular resolution data, we used two different methods, which are described below.

4.1.1 Aperture photometry

We used aperture photometry of the galaxy nucleus in the *Spitzer* and *Herschel* images. The photometry was carried out with the DIGIPHOT package of IRAF. We used different apertures (multiples of the FWHM in each band, see Table 5) and the sky subtraction was carried out using a concentric ring large enough to exclude the

Table 4. Total fluxes measured for NGC 2992, NGC 2993 and Arp 245N in mJy. The flux errors are the result of adding quadratically the calibration uncertainties [3 per cent for IRAC (IRAC Instrument Handbook 2013), 4 per cent for MIPS at 24 μm (MIPS Instrument Handbook 2011), 5 per cent for PACS (PACS Observer's Manual 2013) and 5.5 per cent for SPIRE (SPIRE Handbook 2014)] and the estimated uncertainty for aperture photometry (∼10 per cent). Note that in the case of SPIRE, extended sources have an additional 4 per cent error due to uncertainty in the measurement of the beam area.

	3.6 μm	4.5 μm	5.8 μm	8 μm	24 μm	70 μm	100 μm	160 μm	250 μm	350 μm	500 μm
NGC 2992	180 ± 19	158 ± 19	244 ± 25	510 ± 53	1000 ± 108	9070 ± 1014	12 018 ± 1344	10 794 ± 1207	3882 ± 443	2104 ± 240	357 ± 41
NGC 2993	55 ± 6	41 ± 4	132 ± 14	527 ± 60	1182 ± 127	12 138 ± 1357	13 880 ± 1552	10 776 ± 1205	3291 ± 376	1714 ± 196	291 ± 33
Arp 245N	7 ± 1	4 ± 1	8 ± 1	22 ± 2	3 ± 1	77 ± 9	163 ± 18	394 ± 44	279 ± 32	176 ± 20	31 ± 4

Table 5. NGC 2992 nuclear fluxes calculated using aperture photometry and PSF subtraction (all fluxes in mJy units). Columns 1 and 2 list the instrument/band and its central wavelength (μm). Columns 3 and 4 correspond to each band resolution in arcsec and parsecs. Columns 5 and 6 list the aperture photometry fluxes and corresponding errors, with the aperture photometry carried out in an aperture equals to two FWHM (See Section 4.1.1). Column 7 corresponds to the fluxes obtained from 100 per cent PSF substraction, and columns 8, 9 and 10 list the best percentage of PSF subtraction used in each band, corresponding fluxes and errors. The flux errors are the result of adding quadratically the flux calibration uncertainties (see Table 4) and the errors associated with either aperture photometry (∼10 per cent) or PSF subtraction (∼15 per cent).

Instrument/ Band	Wavelength λ_c (μm)	FWHM (arcsec)	FWHM (pc)	Aperture photometry flux	Flux uncertainty (per cent)	100 per cent PSF substraction flux	Best PSF substraction (per cent)	Best PSF substraction flux	Flux uncertainty (per cent)
IRAC/Ch1	3.6	1.85	322	61	10	59	95	56	15
IRAC/Ch2	4.5	1.77	308	78	10	76	95	73	15
IRAC/Ch3	5.8	2.15	374	148	10	148	80	119	15
IRAC/Ch4	8.0	2.79	485	261	10	272	50	136	15
MIPS/Ch1	24	6.13	1067	874	11	905	90	815	16
PACS/Blue	70	5.25	914	5852	11	3929	60	2357	16
PACS/Green	100	6.75	1175	8080	11	5417	60	3250	16
PACS/Red	160	10.80	1879	7910	11	6135	80	4908	16
SPIRE/PSW	250	17.63	3068	2805	11	2446	65	1590	16
SPIRE/PMW	350	24.49	4261	1608	11	1607	70	1125	16
SPIRE/PLW	500	34.66	6031	287	11	263	75	197	16

galaxy emission. We finally applied corresponding aperture corrections in order to recover the unresolved galaxy flux. These correction factors were computed from the extended Point Response Functions (PRFs) for IRAC,[5] the core PRF for MIPS (see footnote 5) and synthetic PSFs for *Herschel*/ PACS[6] and SPIRE.[7] We performed aperture photometry on the PRFs and PSFs stars, using the same apertures as for the galaxy in each band, and calculated the different correction factors by comparing each individual value with the total flux, measured in an aperture large enough to contain all the star flux. Note that the synthetic PSFs have different pixel scales than the science data and we used the MAGNIFY task of IRAF to resample the PSF images.

We took multiples of the FWHM and then we applied aperture corrections for each one. We find that the aperture corrections converged around 2 FWHM, and then chose this aperture to estimate the nuclear fluxes. In Table 5 and Fig. 8, we show the nuclear galaxy fluxes calculated using this method and including aperture corrections.

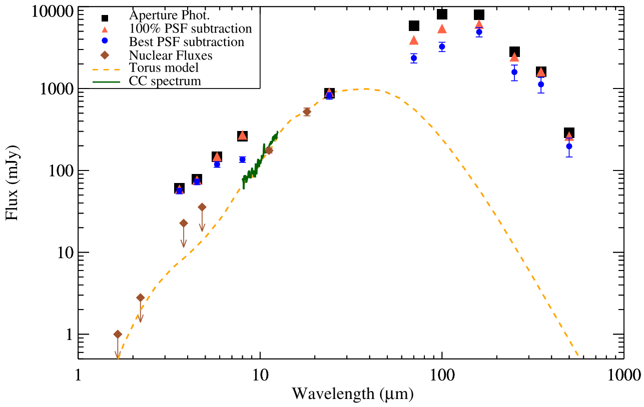

Figure 8. Nuclear fluxes of NGC 2992 from low angular resolution data calculated using aperture photometry (squares) and PSF subtraction at various levels (triangles and circles). The nuclear IR SED (diamonds), including the GTC/CC spectrum and the torus model fitted in Section 3.1.3, are shown for comparison.

4.1.2 *Subtraction of scaled PSFs*

As the aperture photometry might include contamination from the foreground galaxy, here we use the PRF and PSF stars to obtain more realistic nuclear fluxes. First, we scaled the PSF stars to the peak of the galaxy emission in each band, which represents the maximum contribution of the unresolved source, and we integrated the flux in an aperture large enough to contain all the star flux. Then, the host galaxy contribution corresponds to the total galaxy emission minus the scaled PSF (i.e. the residual of the subtraction). We require a relatively flat profile in the residual for a realistic galaxy profile and therefore reduce the scale of the PSF from matching the peak of the galaxy emission to obtain the unresolved fluxes, as in Radomski et al. (2002) and Ramos Almeida et al. (2009). Fig. 9 shows an example of PSF subtraction at various levels (in 3σ contours) for the 160 μm Heschel/PACS image. In this case 80 per cent PSF subtraction produces a flatter profile than 90 and 100 per cent, which are clearly oversubtracted.

The nuclear fluxes calculated using this method are shown in Table 5 and Fig. 8. We also included the results from 100 per cent PSF subtraction, which are more similar to the aperture photometry fluxes, calculated in Section 4.1.1. We note that the relatively flat profile required to determine the best PSF subtraction level might not be completely flat due to possible diffuse or irregular dust structures (Muñoz-Mateos et al. 2009). This potential issue could be affecting the fluxes calculated using this method.

In Fig. 8, we compare the high angular resolution SED and the MAP torus model (see Fig. 4) with those from aperture photometry and PSF subtraction. The latter includes 100 per cent and best PSF subtraction, where the percentage of the best PSF subtraction corresponds to the one that produces the flattest galaxy profile in each band. The best PSF subtraction fluxes are the smallest, but still significantly larger than the high angular resolution SED. Therefore, we find that we cannot recover the nuclear SED from the *Spitzer* and *Herschel* data, with the exception of the 24 μm flux, which we

---

[5] http://irsa.ipac.caltech.edu/data/SPITZER/docs/

[6] ftp://ftp.sciops.esa.int/pub/hsc-calibration/PACS/PSF/

[7] ftp://ftp.sciops.esa.int/pub/hsc-calibration/SPIRE/PHOT/

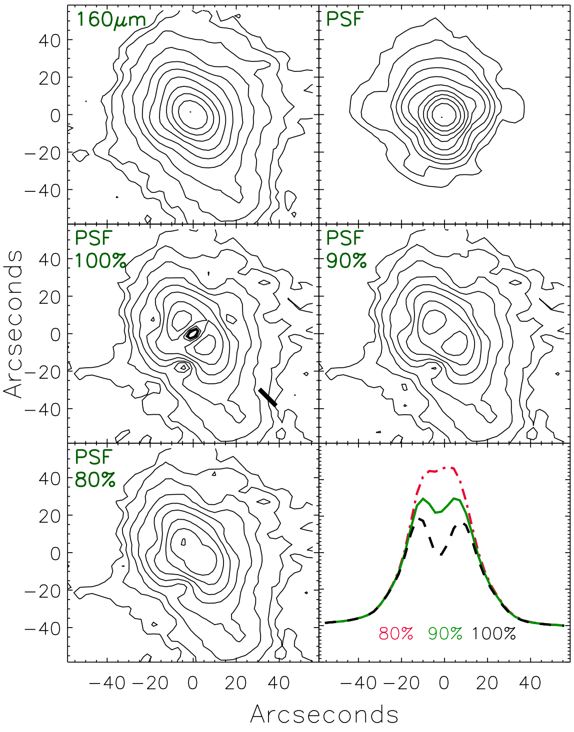

Figure 9. 160 µm Heschel/PACS contours of NGC 2992, the PSF star and the scaled PSF subtraction at the 80, 90 and 100 per cent levels (red dot–dashed, solid green and black dashed lines, respectively). The best subtraction is 80 per cent, according to the flat galaxy profile shown in the bottom-right panel. North is up, and east to left.

recover with both methods. This is expected, since at 20–25 µm the torus emission is supposed to dominate (see Ramos Almeida et al. 2011c and references therein). At shorter and longer wavelengths the galaxy contribution increases and contaminates our aperture photometry and PSF subtracted fluxes.

4.2 Spectral decomposition

Considering the spatial scales probed by the *Spitzer*/IRS spectrum of NGC 2992 (∼630 pc) and the prominent 11.3 µm PAH feature shown in Fig. 3, we expect contributions from the AGN and SF on these scales. To estimate the AGN contribution to the *Spitzer*/IRS spectrum, we take the simple approach of decomposing it in AGN and SB components. To do that, we used the average spectrum of local SB of Brandl et al. (2006) and the templates of purely star-forming LIRGs of Rieke et al. (2009), which cover the IR luminosity range $10 \leq \log(L_{\rm IR}/{\rm L}_{\odot}) \leq 12$. As AGN template, we used the MAP clumpy torus model (i.e. the best-fitting model) fitted in Section 3.1.3, and shown in Fig. 4. The fitting procedure is described in detail in Alonso-Herrero et al. (2012b).

The fit was carried out in the spectral range 6–30 µm to avoid the slightly decreased S/N of the longest wavelengths. We tried different combinations of AGN+SB templates, allowing rescaling of the two components. We finally chose the fit that minimized the χ^2, which in this case was the SB template of IR luminosity $\log(L_{\rm IR}/{\rm L}_{\odot}) = 10$ of Rieke et al. (2009), in combination with the AGN. This IR luminosity is indeed similar to that of NGC 2992 ($\log(L_{\rm IR}/{\rm L}_{\odot}) = 10.52$; Sanders et al. 2003). The result of the fit is shown in the left-hand panel of Fig. 10. We have quantified the AGN fractional contributions to the total 6, 20 and 30 µm emission and obtained 34, 88 and 81 per cent, respectively. We note that the scaled AGN template coincides with the nuclear GTC/CC spectrum within the errors, proving the reliability of the method employed here.

By using this method, we are taking advantage of the privileged information of the high angular resolution GTC/CC spectrum. Therefore, we repeated the same process without using this information and we tried to recover the AGN and SF contributions using the average Seyfert 2 CLUMPY torus model fit reported by Ramos Almeida et al. (2011c) as initial AGN template. In this case the fitted AGN component does not match the high angular resolution GTC/CC spectrum and therefore it is necessary to perform an iterative process to obtain a reliable fit. After the first fit, we subtracted the SB template from the *Spitzer*/IRS spectrum, and then fitted the residual with BayesClumpy. We then performed a second fit using the latter MAP model and the SB templates and repeated the process until the solution converged. To quantify that, we used the AGN fractional contributions at the wavelengths listed before. The percentages at 20 and 30 µm converged after the fourth iteration, but at 6 µm convergence is not reached. This is due to the prominent PAH features at 6.2, 7.7 and 8.6 µm of the SB template, which results in a overestimation of the PAHs contribution to the *Spitzer*/IRS spectrum at these wavelengths. The result of this iterative process is shown in the right-hand panel of Fig. 10. The AGN fractional contributions to the total 6, 20 and 30 µm emission are 43, 88 and 85 per cent, respectively. Therefore, we recover the AGN spectrum of NGC 2992 using only the generic torus models from Ramos Almeida et al. (2011c), and we obtain practically identical AGN fractional contributions at 20 and 30 µm using the two methods described here.

The contribution from SF to the Spizer/IRS spectrum of NGC 2992 is concentrated on the PAH features at 6.2, 7.7, 8.6 and 11.3 µm, as shown Fig. 10. At shorter wavelengths ($\lambda \lesssim 15$ µm) the SB component is stronger than the AGN component, with a ∼60–70 per cent contribution at 6 µm. However, at longer wavelengths ($\lambda \gtrsim 15$ µm) the AGN becomes dominant, reaching ∼90 per cent at 20–25 µm. At $\lambda > 25$ µm, the AGN contribution slowly decreases (see also next section), in agreement with the results reported by Mullaney et al. (2011) for a sample of intermediate luminosity AGN ($L_{2\text{–}10\,\rm keV} \sim 10^{42\text{–}44}$ erg s^{-1}), whose 6–100 µm SEDs are best described by a broken power law that generally peaks between 15–20 µm, and finally falls strongly at $\lambda \gtrsim 40$ µm.

5 PHYSICAL PARAMETERS OF THE CIRCUMNUCLEAR DUST EMISSION OF THE SYSTEM

Dust grains in Seyfert galaxies are heated mainly by SF and nuclear activity, and this radiation is re-emitted in the IR range. The physical properties of large dust grains can be accurately described by a single modified blackbody (Bianchi 2013), and this dust component, heated by the interstellar radiation field, would contain the bulk of the dust mass in a galaxy (Dale et al. 2012). On the other hand, the physical properties of smaller dust grains, i.e. those producing warmer components, are better described by a blend of multiple modified blackbodies with different temperatures (Draine & Li 2007).

For the sake of simplicity, here we will consider single components to describe the shape of the FIR SEDs of NGC 2992 and NGC 2993. This is a similar approach to that used by Pérez García & Rodríguez Espinosa (2001) and Prieto & Acosta-Pulido (2003) to reproduce the IR SED of Seyfert galaxies as the sum of three components: (1) a warm dust component, produced by dust heated

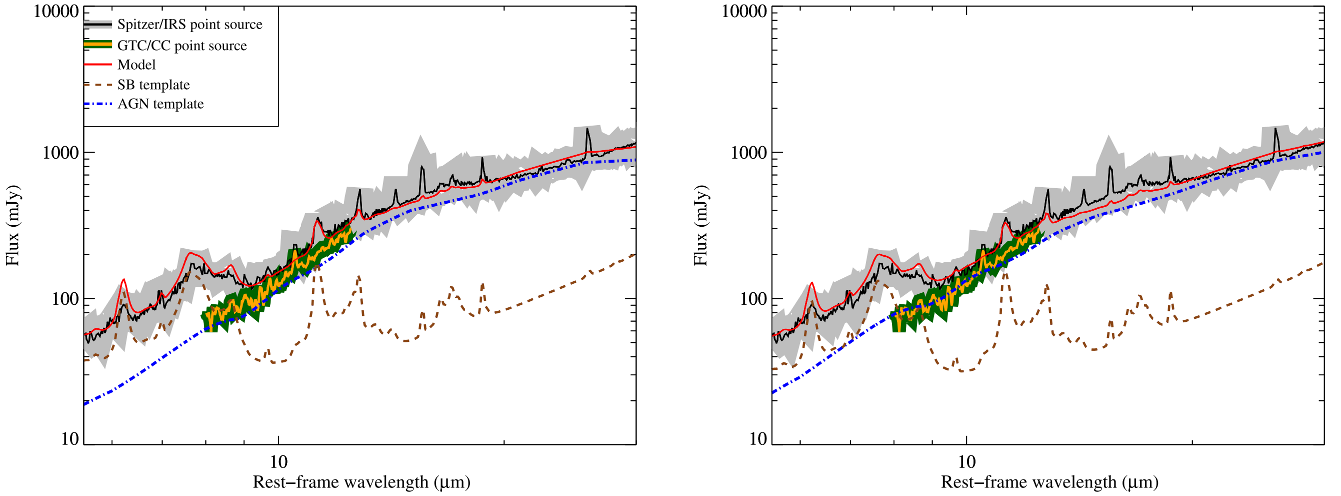

Figure 10. NGC 2992 6–30 μm *Spitzer*/IRS rest-frame spectrum (black solid line), best fit (red solid line), MAP torus model (blue dot–dashed line), and SB template (brown dashed line). Left-hand panel: fit using the MAP torus model fitted to the high angular resolution IR SED of NGC 2992. Right-hand panel: fit using the average Seyfert 2 torus model fit from Ramos Almeida et al. (2011c) and applying an iterative process. The 8–13 μm GTC/CC rest-frame spectrum is shown in both panels for comparison (smoothed with a 2 pixel box; orange line). The uncertainties of the *Spitzer*/IRS and GTC/CC spectra are shown as grey and dark green shaded regions, respectively.

by SF and/or nuclear activity at $T \sim 120$–170 K; (2) a cold component ($T \sim 30$–70 K), associated with SF regions; and (3) a very cold component ($T \sim 15$–25 K), produced by dust heated by the interstellar radiation field. The warm component peaks in the MIR range, and both the cold and very cold dust components are detected in the FIR range.

In the case of the galaxies NGC 2992/93, we consider two different regions to separate the circumnuclear emission from the diffuse and more extended disc emission, as we did in Ramos Almeida et al. (2011b) for the Seyfert 2 galaxy NGC 3081. The circumnuclear region is delimited by a circular aperture of ∼35 arcsec diameter (∼6 kpc), coincident with the largest FWHM of the *Herschel* data (i.e. SPIRE 500 μm; blue solid circles in Fig. 11). We first extracted *Herschel*/PACS and SPIRE fluxes within such aperture and then subtracted the corresponding galaxy background measured in an adjacent annulus (brown dot–dashed circles in Fig. 11). In the case of the active galaxy NGC 2992 we also subtracted the torus model emission (described in Section 3.1.3), which is the main contributor to the warm dust component in this galaxy. The circumnuclear fluxes are represented as red squares in Fig. 12 and reported in Table 6.

The disc emission is computed as the difference between the total fluxes reported in Table 4 (calculated in apertures of 120 arcsec diametre; black dashed circles in Fig. 11) minus the circumnuclear fluxes. These values are plotted as green circles in Fig. 12 and reported in Table 6.

In order to quantify the temperatures and dust masses of the two components described above, we used the following relation: $M_{\rm dust} = D^2 f_\nu / \kappa_\nu B(T)$ (Hildebrand 1983; Bianchi 2013) to fit the FIR SEDs. D is the luminosity distance to the galaxy, f_ν the flux density, κ_ν the absorption opacity of the dust at frequency ν,[8] and $B(T)$ the Planck function evaluated at temperature T.

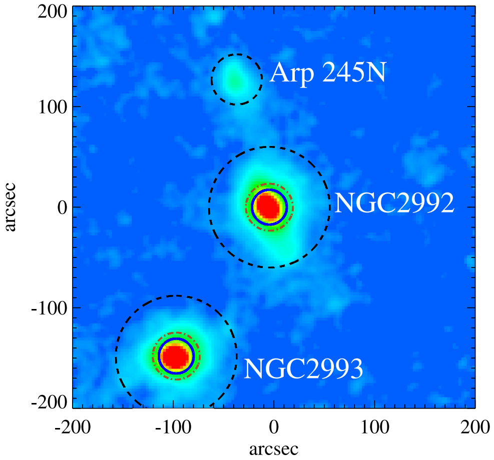

Figure 11. Schema of the different apertures used to calculate the circumnuclear and disc emission of NGC 2992/93, and the total flux of Arp 245N. The apertures are overplotted on the 160 μm Heschel/PACS image of the system. Blue solid and brown dot–dashed circles correspond to the apertures used to calculate the fluxes of the circumnuclear component and the galaxy background that we subtract from the former to get rid of the underlying disc emission. Black dashed circles correspond to the apertures used to calculate the total galaxy fluxes reported in Table 4. The disc emission is calculated by subtracting the circumnuclear fluxes from the total emission.

The fits to the circumnuclear and disc FIR SEDs of NGC 2992/93 are shown in the top and central panels of Fig. 12.[9] The best fits correspond to dust temperatures of 29 ± 1 K and 33 ± 1 K, respectively (see Table 6). These temperatures explain the similarity between the total MIR-to-FIR SEDs of the two spiral galaxies (see Fig. 7). On the other hand, the SEDs of the discs can be described by a dust component of 21 ± 1 K and 22 ± 1 K, respectively (see Table 6). These temperatures coincide with the lowest values

---

[8] The average absorption cross-section is available at http://www.astro.princeton.edu/~draine/dust/dustmix.html. In this paper, we use the $R_V = 3.1$ MW dust model. See Li & Draine (2001) for further details.

[9] Note that we excluded the circumnuclear SPIRE 500 μm fluxes from the fits, as they are underestimated because the circumnuclear aperture does not include an important part of the unresolved flux in this band.

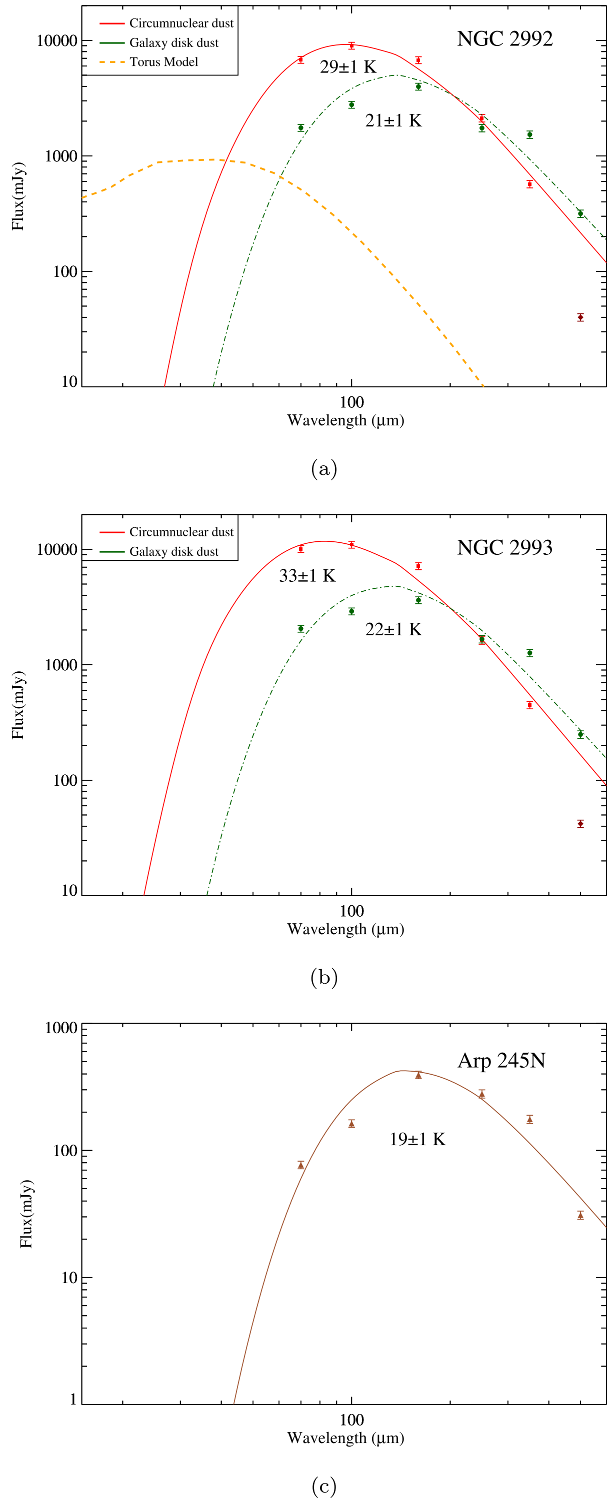

Figure 12. Top and central panels: fits to the circumnuclear and disc SEDs of NGC 2992/93 (red solid and green dot–dashed lines, respectively). The MAP torus model fitted in Section 3.1.3 is also shown in the case of NGC 2992 (orange dashed line). Bottom panel: SED fit of Arp 245N (solid brown line). Note that in the top and central panels, we represent the circumnuclear SPIRE 500 μm fluxes as dark red diamonds, which are excluded from the fits because they are clearly underestimated (see Section 5).

reported by Skibba et al. (2011) for the nearby galaxies in the KINGFISH *Herschel* survey ($T \sim$ 20–35 K). They are also consistent with the values measured for the coldest dust components of Seyfert galaxies (e.g. Radovich et al. 1999; Bendo et al. 2010; Ramos Almeida et al. 2011b) using *Herschel* data as in this study.

The dust masses that we measure for the two components are reported in Table 6. We obtain similar values for the two spiral galaxies: ~5–8 × 10^6 $M_\odot$ and ~15–20 × 10^6 $M_\odot$ for the circumnuclear and galaxy disc components, respectively, with those of NGC 2992 being slightly larger. These dust masses are within the lowest values reported by da Cunha et al. (2010) for a sample of star-forming galaxies, using the $M_{\rm dust}$-star formation rate (SFR) relation ($M_{\rm d} \sim$ 10–100× 10^6 $M_\odot$ for the galaxies with the highest S/N of the sample).

We also measured total fluxes for the dwarf galaxy Arp 245N in an aperture radius of 25 arcsec, after subtracting the sky background (see Table 6 and Fig. 11).[10] These fluxes are plotted as brown triangles in the bottom panel of Fig. 12, and fitted using a temperature of 19 ± 1 K and a total dust mass of $M_{\rm dust} = (3.2 \pm 1.1) \times 10^6$ $M_\odot$. This low temperature is compatible with dust heated by the interstellar radiation field and the relatively weak MIR emission of the galaxy in the range ~24–100 μm(see Fig. 7) would be indicating that a significant part of the old stellar population and the interstellar medium of NGC 2992 and NGC 2993 have been stripped from the galaxies during the interaction process undergone by the system.

Finally, we estimated SFRs for the three galaxies in the system using the 70 μm fluxes reported in Table 6 and equation 14 in Rieke et al. (2009). We decided to use the 70 μm fluxes because the 24 μm flux is dominated by the AGN contribution in the case of NGC 2992. However, we checked that we obtain similar SFR estimations for NGC 2993 and Arp 245N when using 24 and 100 μm fluxes. The SFRs that we measure for the two spiral galaxies are very similar considering the errors (see Table 6). For Arp 245N we derive a small SFR (~0.03 $M_\odot$ yr^{-1}), consistent with the low temperature of the dust and the weak MIR emission.

6 DISCUSSION

6.1 NGC 2992

NGC 2992 contains a Seyfert 1.9 nucleus, although it has changed its type between Seyfert 1.5 and 2 and it has also exhibited huge variations across all the spectrum (Trippe et al. 2008). The 2–10 keV X-ray luminosity dramatically decreased between 1978 and 1994 (a factor of ~16; see Table 3) and then increased by roughly the same amount from 1994 to 2005 (Gilli et al. 2000; Yaqoob et al. 2007; Brightman & Nandra 2011). Besides, Glass (1997) reported variability in the NIR, with the source fading from 1978 to 1996, except for a strong outburst in 1988. This IR variability mirrors that detected in the X-ray regime, with the corresponding delay due to the different scales that each emission is probing (Clavel, Wamsteker & Glass 1989; Barvainis 1992; Hönig & Kishimoto 2011). Gilli et al. (2000) explained the extreme variability of NGC 2992 as caused by a retriggered AGN, and in particular, by different stages of the rebuilding of the accretion disc, which the latter authors estimated to range between 1 and 5 yr.

According to the new observations reported here, the nuclear MIR spectrum of NGC 2992 has not changed either in flux or shape from 2007 to 2014. This is in agreement with the scenario proposed

---

[10] These fluxes are same as those reported in Table 4.

Table 6. Fluxes of the circumnuclear (a) and disc (b) components of NGC 2992 and NGC 2993 described in Section 5, total fluxes of Arp 245N and physical properties derived from the SED fits shown in Fig. 12. See Fig. 11 for further details on the different apertures employed.

	70 μm (mJy)	100 μm (mJy)	160 μm (mJy)	250 μm (mJy)	350 μm (mJy)	500 μm (mJy)	Temperature (K)	$M_{\rm dust}$ (10^6 M$_\odot$)	SFR (M$_\odot$ yr^{-1})
NGC 2992 (a)	6801 ± 1075	9013 ± 1424	6759 ± 1068	2124 ± 363	570 ± 97	40 ± 7	29 ± 1	7.6 ± 1.3	2.5 ± 0.4
NGC 2992 (b)	1751 ± 277	2776 ± 439	3981 ± 629	1743 ± 298	1530 ± 262	316 ± 54	21 ± 1	19.6 ± 2.7	0.7 ± 0.1
NGC 2993 (a)	10083 ± 1593	10979 ± 1735	7153 ± 1130	1625 ± 278	488 ± 83	42 ± 7	33 ± 1	4.7 ± 0.8	3.7 ± 0.6
NGC 2993 (b)	2055 ± 325	2902 ± 459	3623 ± 572	1666 ± 285	1266 ± 216	249 ± 43	22 ± 1	14.9 ± 2.0	0.8 ± 0.1
Arp 245N	77 ± 9	163 ± 18	394 ± 44	279 ± 32	176 ± 20	31 ± 4	19 ± 1	3.2 ± 1.1	~0.03

by Gilli et al. (2000), in which the rebuilding of the accretion disc would have been finished in 2005, first stopping the X-ray variability and finally, the IR variability. Monitoring campaigns in the X-ray and the optical/IR are then key to constrain the relative sizes of the AGN internal structures as well as to understand the physics of nuclear activity.

In Section 3.1.3, we derived a column density of $N_{\rm H} \sim 10^{24}$ cm^{-2} from the fit of the nuclear SED with clumpy torus models. This column density is much higher than the values derived from X-ray measurements, as e.g. the $N_{\rm H} \sim 10^{22}$ cm^{-2} reported by Gilli et al. (2000) or the $N_{\rm H} = 8 \times 10^{21}$ cm^{-2} reported by Yaqoob et al. (2007). However, Weaver et al. (1996) measured a narrow and prominent Fe Kα line with a large EW (~500eV) from X-ray data taken with the *Advanced Satellite for Cosmology and Astrophysics* (*ASCA*). The strong Fe Kα line and the Compton-reflection component inferred by Weaver et al. (1996) require the existence of cold dense gas with a column of density of $N_{\rm H} \sim 10^{23}$–10^{25} cm^{-2}, which comprises the value derived from our fit. Moreover, Weaver et al. (1996) associated the lag in the response of these X-ray features to changes in continuum flux, from which they estimated the reprocessor size to be ~ 3 pc. This is roughly in agreement with the torus size derived from our fit ($R_{\rm o} = 1.5 \pm 0.5$ pc). Therefore, a clumpy torus with the properties derived from the fit performed here is in agreement with the scenario proposed by Weaver et al. (1996). On the other hand, the intermediate covering factor of the torus that we infer from the fit presented in Section 3.1.3 could explain the changes in Seyfert type experienced by NGC 2992 (Trippe et al. 2008).

In Section 4.2, we used clumpy torus models and a set of SB templates to decompose the *Spitzer*/IRS spectrum of NGC 2992, which probes the central kpc of the galaxy. We found an important contribution from SF at short MIR wavelengths ($\lambda \sim 6$–15 μm; 60–70 per cent), which is concentrated on the PAH features at 6.2, 7.7, 8.6 and 11.3 μm. On the other hand, at $\lambda \sim 15$–30 μm, the AGN dominates the *Spitzer*/IRS spectrum, reaching 90 per cent at 20–25 μm. A similar, but more simplistic approach was taken by Deo et al. (2009) using *Spitzer*/IRS data in mapping-mode.[11] They subtracted the average starburst galaxy spectrum from Brandl et al. (2006) from the *Spitzer*/IRS spectrum after scaling it, aiming to completely remove the 11.3 and 17 μm PAH features from the residual. By using this method, they found that the contribution from the SB increases with wavelength, as opposed to what we find using our spectral decomposition technique. We also tried a fit using clumpy torus models and the Brandl et al. (2006) SB template, but the result did not successfully reproduce the *Spitzer*/IRS spectrum. In addition, from the analysis of the IR photometry performed in Section 4 we know that the AGN emission, in the scales probed by *Spitzer*, becomes dominant at 20–25 μm, in agreement with the results derived from spectroscopic data. Finally, using the high angular resolution imaging and spectroscopic data of NGC 2992 presented here, we have shown that SF is either suppressed or diluted by the strong AGN radiation field in the inner ~50 pc of the galaxy (see Section 3.1.2), as shown by the lack of PAH features in the nuclear spectrum.

6.2 The Arp 245 interacting system

As previously mentioned, the interacting system Arp 245 is formed by the two spiral galaxies NGC 2992/93, the dwarf galaxy Arp 245N and two major tidal features. These features consist on two bridges connecting the three galaxies (see Fig. 5). The fact that the tidal features are well developed indicates that the system is seen close after its first encounter (see Duc et al. 2000 and references therein). Furthermore, the northern bridge linking NGC 2992 and Arp 245N is relatively bright and dense, whereas that associated with NGC 2993 appears like a weaker large open ring. The prominence of the two bridges suggests that the two spiral galaxies are experiencing prograde encounters (galaxy spins in the same sense as the flyby; Toomre & Toomre 1972). None the less, the bridges extend ~16 and 27 kpc, respectively, which are rather modest extents compared with the long 100 kpc antennas observed in the prototypical interacting galaxy pair NGC 4038/39. However, these lengths are expected for an interacting system in an early phase such as Arp 245, with the bridges still developing. This is confirmed by the numerical modelling performed by Duc et al. (2000), which predicts that the first galaxy encounter happened ~100 Myr ago.

According to Tadhunter et al. (2011) and Ramos Almeida et al. (2011a), three main stages can be defined in a galaxy merger sequence: (i) pre-coalescence, (ii) coalescence, and (iii) post-coalescence. In the pre-coalescence phase the two nuclei are observed after the first passage, and immediately before (~100 Myr) the coalescence of the two nuclei. The peak of AGN activity is expected during coalescence, although during the pre-coalescence most objects tend to also exhibit AGN or SB activity associated with the gas infall produced by the tidal forces at play. This is indeed the case of the galaxy pair NGC 2992/93: NGC 2992 is known to host a Seyfert nucleus, and all the galaxies show circumnuclear SF, as revealed by their FIR luminosities (see Section 3.2) and the Hα imaging presented in Duc et al. (2000).

A more recent study on interacting systems is presented in Lanz et al. (2013), where the authors measured and modelled the galaxy SEDs from the ultraviolet to the FIR, also using *Spitzer* and *Herschel* data to cover the IR range. From this modelling they derived temperatures, dust masses and SFRs for the galaxies in their sample. In addition, Lanz et al. (2013) classify the galaxies in different interaction stages attending to the galaxy morphologies, using a similar classification scheme as in Dopita et al. (2002). They divide the sample in four categories: (1) non-interacting galaxies;

---

[11] In this work, we are using the *Spitzer*/IRS spectrum of NGC 2992 in staring-mode.

(2) galaxies in a weak integrating system, which are close but show minimal morphological distortion; (3) moderately interacting galaxies showing strong sings of morphological disturbance such as tidal tails; and (4) strongly interacting galaxies in a more evolved stage of the interaction.

As explained above, the Arp 245 system would be in the pre-coalescence stage of the interaction, which would correspond to stages 3/4 of the classification employed by Lanz et al. (2013). For these stages they report average dust masses of ∼1–4× 10^7 $M_\odot$, dust temperatures of ∼20–23 K, and SFRs of ∼0.6–7.8 $M_\odot$ yr^{-1}. These values are consistent with the measurements reported in Table 6 for the disc components of NGC 2992/93, being more similar to the stage 3 values, i.e. moderately integrating galaxies showing strong signs of morphological disturbance.

Using the determined dust masses for the spiral galaxies, we derived gas-to-dust ratios[12] of 70 and 50 for NGC 2992 and NGC 2993, respectively. These ratios are comparable to those measured in other nearby galaxies, including active and non-active galaxies. As an example, see the results obtained for the *Spitzer* IR Nearby Galaxies Survey (Draine et al. 2007).

A remarkable feature is the similarity of the MIR-to-FIR (beyond 10 μm) emission coming from the two spiral galaxies (see Fig. 7). They are closely matched in luminosity and spectral shape. We can compare the SFRs derived from our FIR data with those obtained by Duc et al. (2000) from Hα imaging. As expected, the largest contribution to the SFR comes from the circumnuclear region(ratio 4–5:1 relative to the disc). Adding the two contributions, we obtain 3.2 and 4.5 $M_\odot$ yr^{-1} for NGC 2992 and NGC 2993, respectively. Duc et al. (2000) reported Hα luminosities of 1.7 and 2.8× 10^{41} erg s^{-1} for the two spirals, which can be transformed to SFRs, resulting in 0.7 and 1.14 $M_\odot$ yr^{-1} for NGC 2992 and NGC 2993, respectively. We corrected these figures for extinction using $E(B-V) = 0.84$ and 0.7 for NGC 2992/93, measured from the recombination lines (Durret & Bergeron 1988). The extinction-corrected values are 9.1 and 9.8 $M_\odot$ yr^{-1} for NGC 2992 and NGC 2993, respectively, which are larger than the values that we derive here. However, we note that the average extinction correction that we are using may not be adequate, since the integrated Hα emission comes from regions with different levels of obscuration.

All the tidal features observed in the optical images of the Arp 245 system (Duc et al. 2000) have counterparts in the MIR-to-FIR observations presented here (see Fig. 5), although they show different properties. The galaxy Arp 245N, that is clearly detected in the four *Spitzer*/IRAC bands (from 3.6 to 8 μm), becomes much fainter at 24 and 70 μm, and arises again at wavelengths beyond 100 μm. This bimodal emission fits with the hypothesis made by Duc et al. (2000), who proposed this source to be formed by an old stellar population tidally stripped from NGC 2992, plus a minor contribution from young stars formed *in situ* after the interaction. The latter is spectroscopically corroborated by the presence of Hα and Hβ emission. The EW of Hβ emission line indicates that the SB started less than 10 Myr ago (Duc et al. 2000). Using the PACS 70 μm flux of Arp 245N, we derived a relatively low SFR per unit area (ΣSFR): Log ΣSFR∼ $-3.3 M_\odot$ yr^{-1} kpc^{-2}, which is considerably larger than the extinction-corrected value reported by Duc et al. (2000), of -2.5 $M_\odot$ yr^{-1} kpc^{-2}, obtained from the Hα luminosity. This difference could be due to an overestimation of the extinction correction applied by Duc et al. (2000), who measured Log ΣSFR ∼ -3.1 $M_\odot$ yr^{-1} kpc^{-2} before correcting for extinction. The gas-to-dust mass ratio that we measured for Arp 245N is ∼280, which might indicate that this region is a H I reservoir, where the dust content is relatively low, as well as the SF.

The Arp 245 Bridge is only detected at wavelengths longer than 160 μm (see Fig. 5), indicating the presence of very cold dust. There is no evidence for dust heated by SF activity in this feature, which is corroborated by the lack of ionized gas in the Hα images (Duc et al. 2000). The lack of recent SF in the bridge would indicate that the conditions are not adequate, i.e. the H I column density could be below the threshold required for SF to take place.

Summarizing, the MIR-to-FIR maps presented in this work are in good agreement with the system being in an early phase of the interaction between the galaxy pair NGC 2992/93 (∼100 Myr after the first encounter). The MIR-to-FIR luminosities indicate that both spirals are relatively bright IR galaxies, with the SF activity mostly concentrated in the circumnuclear regions. On the other hand, the tidal features have not reached the conditions to be active star-forming sites.

IR studies of interacting systems are important to advance in our understanding of the evolution of the gas/dust properties of such systems as the interaction evolves. Our work contributes to this understanding with the analysis of two spiral galaxies in clear interaction, one of them an AGN, and a dwarf galaxy likely stripped from NGC 2992. The different dust properties of the dwarf galaxy and the two spirals provide one more piece of information about how SF and nuclear activity are triggered in galaxy interactions, but similar studies of other interacting systems in different stages of the interaction, including galaxies of different masses and types, are fundamental to derive general conclusions.

7 CONCLUSIONS

We have presented *Spitzer* and *Herschel* IR imaging of the interacting system Arp 245, and high angular resolution IR imaging and MIR spectroscopic observations of the Seyfert 1.9 galaxy NGC 2992. For NGC 2992, we have used different methods to recover the nuclear emission from the *Spitzer* and *Herschel* data, and compared it with the ground-based IR observations of this galaxy. We have also studied in detail the circumnuclear and disc emission of the Arp 245 system, and reproduced the FIR SEDs of these two regions with dust models, from which we derived dust temperatures and masses. Our major results are as follows.

(i) The ground-based 11.2 μm image of NGC 2992 has an angular resolution of 0.32 arcsec (55 pc) and reveals faint extended emission along PA ∼ 30° and out to ∼3 kpc. The orientation of this extended emission coincides with the semi-major axis of the galaxy.

(ii) The GTC/CC spectrum of the faint MIR extended emission clearly shows the 11.3 μm PAH feature and the [S IV]λ10.5 μm emission line once we remove the AGN contribution. Therefore, we conclude that this extended emission is produced, at least in part, by dust heated by SF. Moreover, by comparing the extended and nuclear spectra of the galaxy we conclude that either the PAH features have been destroyed in the inner ∼50 pc of NGC 2992, or are diluted by the strong AGN continuum.

(iii) The GTC/CC and Gemini/MICHELLE nuclear spectra of NGC 2992, which probe the inner ∼50 pc of the galaxy, are identical in spite of the time difference between the observations (∼7 years) and the different slit orientations. These spectra show [S IV] λ10.5 μm emission and no PAH features. This similarity

---

[12] The H I mass has been taken from Duc et al. (2000). We note that we calculate the gas-to-dust ratios using atomic gas masses, but it is possible that a substantial fraction of the gas mass is in molecular form.

indicates that the X-ray and IR variability previously observed in this galaxy may have stopped after 2007.

(iv) We modelled the nuclear IR SED of NGC 2992 with clumpy torus models, and derived an AGN bolometric luminosity of $L_{\rm bol}^{\rm AGN} = 5.8 \times 10^{43}$ erg s^{-1}, consistent with the value estimated from X-ray data: $L_{\rm bol}^{\rm X-ray} = 3.2 \times 10^{43}$ erg s^{-1}. We infer a small torus radius of ∼1.2 pc from the fit, a torus mass of $M_{\rm torus} = 9 \times 10^4 M_\odot$ and a column density of $N_{\rm H} = 3.4 \times 10^{24}$ cm^{-2}. The latter value is consistent with the range reported from X-ray observations of the inner ∼3 pc of the galaxy.

(v) We calculated nuclear fluxes for NGC 2992 using the *Spitzer* MIR and *Herschel* FIR images and different methods, and we found that we can only recover the nuclear fluxes obtained from high angular resolution data at 20–25 μm, where the AGN emission dominates.

(vi) We decomposed the 5–30 μm *Spitzer*/IRS spectrum, which probes the inner 630 pc of NGC 2992, in AGN and SB components. We found that the SB component dominates the MIR emission at $\lambda \lesssim 15\mu$m, with ∼60–70 per cent contribution at 6 μm. At $\lambda \gtrsim 15$ μm, the AGN component dominates, reaching 90 per cent at 20 μm, and decreasing rapidly at $\lambda > 30$ μm.

(vii) The scaled AGN template derived from the spectral decomposition of the *Spitzer* spectrum agrees well in flux and shape with the GTC/CC nuclear MIR spectrum within the errors, proving the reliability of this method for estimating the SB and AGN contribution to the MIR emission.

(viii) The MIR-to-FIR total SEDs of the interacting galaxies NGC 2992/93 are practically identical in shape and flux. This similarity is likely related to the presence of intense SF in both galaxies, which is heating the dust at similar temperatures.

(ix) We reproduced the FIR emission of the different components of the Arp 245 system using dust models and measured practically the same dust masses, temperatures and SFRs for NGC 2992/93. These measurements are very similar to those reported for non-active interacting systems in the first stages of the interaction.

(x) The MIR-to-FIR maps and cold dust properties presented here are consistent with the Arp 245 system being in an early stage of the interaction between the galaxy pair NGC 2992/93, with the SF activity mostly concentrated in their circumnuclear regions. On the other hand, the tidal features do not seem to have reached the conditions to be active star-forming sites.

ACKNOWLEDGEMENTS

IGB acknowledges financial support from the Instituto de Astrofísica de Canarias through Fundación La Caixa. This research was partly supported by a Marie Curie Intra European Fellowship within the 7th European Community Framework Programme (PIEF-GA-2012-327934). CRA and IGB acknowledge financial support from the Spanish Ministry of Science and Innovation (MICINN) through project PN AYA2013-47742-C4-2-P. AAH acknowledges funding from the Spanish Ministry of Economy and Competitiveness under grant AYA2012-31447, which is party funded by the FEDER program. PE acknowledges support from the Spanish Plan Nacional de Astronomía y Astrofísica under grant AYA2012-31277. OGM acknowledges support from grant AYA2012-39168-C03-01. TDS was supported by ALMA-CONICYT grant number 31130005.

This work is based on observations made with the Gran Telescopio CANARIAS (GTC), installed in the Spanish Observatorio del Roque de los Muchachos of the Instituto de Astrofísica de Canarias, in the island of La Palma.

This research has made use of the NASA/IPAC Extragalactic Database (NED) which is operated by the Jet Propulsion Laboratory, California Institute of Technology, under contract with the National Aeronautics and Space Administration.

Based on observations obtained at the Gemini Observatory, which is operated by the Association of Universities for Research in Astronomy, Inc. under a cooperative agreement with the NSF on behalf of the Gemini partnership: the National Science Foundation (United States), the Science and Technology Facilities Council (United Kingdom), the National Research Council (Canada), CONICYT (Chile), the Australian Research Council (Australia), Ministério da Ciência e Tecnologia (Brazil) and Ministerio de Ciencia, Tecnologia e Innovación Productiva (Argentina).

Based on observations made with the NASA/ESA *HST*, obtained from the data archive at the Space TElescope Science Institute. STScI is operated by the Association of Universities for Research in Astronomy, Inc. under NASA contract NAS 5-26555.

Based on observation made with the *Spitzer Space Telescope*, which is operated by the Jet Propulsion Laboratory, California Institute of Technology, under NASA contract 1407.

Based on observation made with the *Herschel* Observatory, which is an ESA space observatory with science instruments provided by European-led Principal Investigator consortia and with important participation from NASA. PACS has been developed by a consortium of institutes led by MPE (Germany) and including UVIE (Austria); KU Leuven, CSL, IMEC (Belgium); CEA, LAM (France); MPIA (Germany); INAF-IFSI/OAA/OAP/OAT, LENS, SISSA (Italy); IAC (Spain). This development has been supported by the funding agencies BMVIT (Austria), ESA-PRODEX (Belgium), CEA/CNES (France), DLR (Germany), ASI/INAF (Italy) and CICYT/MCYT (Spain). SPIRE has been developed by a consortium of institutes led by Cardiff Univ. (UK) and including Univ. Lethbridge (Canada); NAOC (China); CEA, LAM (France); IFSI, Univ. Padua (Italy); IAC (Spain); Stockholm Observatory (Sweden); Imperial College London, RAL, UCL-MSSL, UKATC, Univ. Sussex (UK); and Caltech, JPL, NHSC, Univ. Colorado (USA). This development has been supported by national funding agencies: CSA (Canada); NAOC (China); CEA, CNES, CNRS (France); ASI (Italy); MCINN (Spain); SNSB (Sweden); STFC, UKSA (UK); and NASA (USA).

The authors are extremely grateful to the GTC staff for their constant and enthusiastic support, specially to Carlos Álvarez. We finally acknowledge useful comments from the anonymous referee.

REFERENCES

Adams T. F., 1977, ApJS, 33, 19
Allen M. G., Dopita M. A., Tsvetanov Z. I., Sutherland R. S., 1999, ApJ, 511, 686
Alonso-Herrero A., Quillen A. C., Simpson C., Efstathiou A., Ward M. J., 2001, AJ, 121, 1369
Alonso-Herrero A. et al., 2011, ApJ, 736, 82
Alonso-Herrero A. et al., 2012a, MNRAS, 425, 311
Alonso-Herrero A., Pereira-Santaella M., Rieke G. H., Rigopoulou D., 2012b, ApJ, 744, 2
Alonso-Herrero A. et al., 2013, ApJ, 779, L14
Alonso-Herrero A. et al., 2014, MNRAS, 443, 2766
Antonucci R., 1993, ARA&A, 31, 473
Asensio Ramos A., Ramos Almeida C., 2009, ApJ, 696, 2075
Asensio Ramos A., Ramos Almeida C., 2013, MNRAS, 428, 195
Barvainis R., 1992, ApJ, 400, 502

Bendo G. J. et al., 2010, A&A, 518, L65

Bessiere P. S., Tadhunter C. N., Ramos Almeida C., Villar Martín M., 2012, MNRAS, 426, 276

Bianchi S., 2013, A&A, 552, AA89

Bohlin R. C., Savage B. D., Drake J. F., 1978, ApJ, 224, 132

Brandl B. R. et al., 2006, ApJ, 653, 1129

Brightman M., Nandra K., 2011, MNRAS, 413, 1206

Burtscher L. et al., 2013, A&A, 558, A149

Chapman S. C., Morris S. L., Alonso-Herrero A., Falcke H., 2000, MNRAS, 314, 263

Chiar J. E., Tielens A. G. G. M., 2006, ApJ, 637, 774

Clavel J., Wamsteker W., Glass I. S., 1989, ApJ, 337, 236

Colbert E. J. M., Baum S. A., Gallimore J. F., O'Dea C. P., Lehnert M. D., Tsvetanov Z. I., Mulchaey J. S., Caganoff S., 1996, ApJS, 105, 75

Colbert E. J. M., Baum S. A., O'Dea C. P., Veilleux S., 1998, ApJ, 496, 786

Colina L., Fricke K. J., Kollatschny W., Perryman M. A. C., 1987, A&A, 178, 51

Colling M., 2011, PhD thesis, Univ. Oxford

da Cunha E., Eminian C., Charlot S., Blaizot J., 2010, MNRAS, 403, 1894

Dale D. A. et al., 2012, ApJ, 745, 95

Dale D. A., Helou G., Magdis G. E., Armus L., Díaz-Santos T. Shi. Y., 2014, ApJ, 784, 83

Dasyra K. M., Ho L. C., Netzer H., Combes F., Trakhtenbrot B., Sturm E., Armus L., Elbaz D., 2011, ApJ, 740, 94

de Vaucouleurs G., de Vaucouleurs A., Corwin H. G., Buta R. J., Jr, Paturel G., Fouqué P., 1991, Third Reference Catalogue of Bright Galaxies. Springer, New York

Deo R. P., Richards G. T., Crenshaw D. M., Kraemer S. B., 2009, ApJ, 705, 14

Dopita M. A., Pereira M., Kewley L. J., Capaccioli M., 2002, ApJS, 143, 47

Draine B. T., Li A., 2007, ApJ, 657, 810

Draine B. T. et al., 2007, ApJ, 663, 866

Duc P.-A., Brinks E., Springel V., Pichardo B., Weilbacher P., Mirabel I. F., 2000, AJ, 120, 1238

Durret F., Bergeron J., 1987, A&A, 173, 219

Durret F., Bergeron J., 1988, A&AS, 75, 273

Elvis M. et al., 1994, ApJS, 95, 1

Esquej P. et al., 2014, ApJ, 780, 86

Fazio G. G. et al., 2004, ApJS, 154, 10

García-Burillo S. et al., 2014, A&A, 567, A125

García-Lorenzo B., Arribas S., Mediavilla E., 2001, A&A, 378, 787

Gilli R., Maiolino R., Marconi A., Risaliti G., Dadina M., Weaver K. A., Colbert E. J. M., 2000, A&A, 355, 485

Glass I. S., 1997, MNRAS, 292, L50

Glasse A. C., Atad-Ettedgui E. I., Harris J. W., 1997, in Ardeberg A. L., ed., Proc. SPIE Conf. Ser. Vol. 2871, Optical Telescopes of Today and Tomorrow. SPIE, Bellingham, p. 1197

González-Martín O. et al., 2013, A&A, 553, A35

Griffin M. J. et al., 2010, A&A, 518, L3

Hildebrand R. H., 1983, QJRAS, 24, 267

Hönig S. F., Kishimoto M., 2010, A&A, 523, A27

Hönig S. F., Kishimoto M., 2011, A&A, 534, A121

Hopkins P. F., Quataert E., 2010, MNRAS, 407, 1529

Hopkins P. F., Cox T. J., Kereš D., Hernquist L., 2008, ApJS, 175, 390

Houck J. R. et al., 2004, ApJS, 154, 18

Howell J. H. et al., 2007, AJ, 134, 2086

IRAC Instrument and Instrument Support Teams 2013, IRAC Instrument Handbook 2013, Version 2.0.3, SSC, Pasadena

Jarrett T. H., Chester T., Cutri R., Schneider S. E., Huchra J. P., 2003, AJ, 125, 525

Lanz L. et al., 2013, ApJ, 768, 90

Lebouteiller V., Barry D. J., Spoon H. W. W., Bernard-Salas J., Sloan G. C., Houck J. R., Weedman D. W., 2011, ApJS, 196, 8

Li A., Draine B. T., 2001, ApJ, 554, 778

Lípari S., Mediavilla E., Díaz R. J., García-Lorenzo B., Acosta-Pulido J., Agüero M. P., Terlevich R., 2004, MNRAS, 348, 369

Lira P., Videla L., Wu Y., Alonso-Herrero A., Alexander D. M., Ward M., 2013, ApJ, 764, 159

McLeod B., 1997, in Casertano S., Jedrzejewski R., Keyes T., Stevens M., eds, Proc. 1997 HST Calibration Workshop, The 1997 HST Calibration Workshop with a New Generation of Instruments. STSci, Baltimore, p. 281

Malkan M. A., Gorjian V., Tam R., 1998, ApJS, 117, 25

Marinucci A., Bianchi S., Nicastro F., Matt G., Goulding A. D., 2012, ApJ, 748, 130

Mason R. E., Geballe T. R., Packham C., Levenson N. A., Elitzur M., Fisher R. S., Perlman E., 2006, ApJ, 640, 612

Mason R. E., Levenson N. A., Shi Y., Packham C., Gorjian V., Cleary K., Rhee J., Werner M., 2009, ApJ, 693, L136

MIPS Instrument and MIPS Instrument Support Teams 2011, MIPS Instrument Handbook, Version 3, SSC, Pasadena

Mullaney J. R., Alexander D. M., Goulding A. D., Hickox R. C., 2011, MNRAS, 414, 1082

Müller-Sánchez F., Prieto M. A., Hicks E. K. S., Vives-Arias H., Davies R. I., Malkan M., Tacconi L. J., Genzel R., 2011, ApJ, 739, 69

Muñoz-Mateos J. C. et al., 2009, ApJ, 701, 1965

Mushotzky R. F., 1982, ApJ, 256, 92

Nandra K., Pounds K. A., 1994, MNRAS, 268, 405

Nenkova M., Sirocky M. M., Ivezić Ž., Elitzur M., 2008a, ApJ, 685, 147

Nenkova M., Sirocky M. M., Nikutta R., Ivezić Ž., Elitzur M., 2008b, ApJ, 685, 160

Nikutta R., Elitzur M., Lacy M., 2009, ApJ, 707, 1550

Ott S., 2010, in Mizumoto Y., Morita K.-I., Ohishi M., eds, ASP Conf. Ser. Vol. 434, Astronomical Data Analysis Software and Systems XIX. Astron. Soc. Pac., San Francisco, p. 139

Packham C., Radomski J. T., Roche P. F., Aitken D. K., Perlman E., Alonso-Herrero A., Colina L., Telesco C. M., 2005, ApJ, 618, L17

PACS Observer's Manual 2013, Version 2.5.1, HERSCHEL-HSC-DOC-0832. Herschel Science Centre

Pereira-Santaella M., Alonso-Herrero A., Rieke G. H., Colina L., Díaz-Santos T., Smith J.-D. T., Pérez-González P. G., Engelbracht C. W., 2010, ApJS, 188, 447

Pérez García A. M., Rodríguez Espinosa J. M., 2001, ApJ, 557, 39

Pilbratt G. L. et al., 2010, A&A, 518, L1

Poglitsch A. et al., 2010, A&A, 518, L2

Prieto M. A., Acosta-Pulido J. A., 2003, ApJ, 583, 689

Quillen A. C., Alonso-Herrero A., Rieke M. J., Rieke G. H., Ruiz M., Kulkarni V., 1999, ApJ, 527, 696

Radomski J. T., Piña R. K., Packham C., Telesco C. M., Tadhunter C. N., 2002, ApJ, 566, 675

Radomski J. T., Piña R. K., Packham C., Telesco C. M., De Buizer J. M., Fisher R. S., Robinson A., 2003, ApJ, 587, 117

Radovich M., Klaas U., Acosta-Pulido J., Lemke D., 1999, A&A, 348, 705

Ramos Almeida C. et al., 2009, ApJ, 702, 1127

Ramos Almeida C., Dicken D., Tadhunter C., Asensio Ramos A., Inskip K. J., Hardcastle M. J., Mingo B., 2011a, MNRAS, 413, 2358

Ramos Almeida C. et al., 2011b, MNRAS, 417, L46

Ramos Almeida C. et al., 2011c, ApJ, 731, 92

Ramos Almeida C. et al., 2012, MNRAS, 419, 687

Ramos Almeida C. et al., 2014, MNRAS, 445, 1130

Rieke G. H. et al., 2004, ApJS, 154, 25

Rieke G. H., Alonso-Herrero A., Weiner B. J., Pérez-González P. G., Blaylock M., Donley J. L., Marcillac D., 2009, ApJ, 692, 556

Roussel H., 2012, Astrophysics Source Code Library, record ascl:1209.012

Sanders D. B., Mazzarella J. M., Kim D.-C., Surace J. A., Soifer B. T., 2003, AJ, 126, 1607

Serra P., Trager S. C., van der Hulst J. M., Oosterloo T. A., Morganti R., 2006, A&A, 453, 493

Shu X. W., Yaqoob T., Murphy K. D., Braito V., Wang J. X., Zheng W., 2010, ApJ, 713, 1256

Skibba R. A. et al., 2011, ApJ, 738, 89

SPIRE Handbook 2014, Version 2.5, HERSCHEL-HSC-DOC-0798. Herschel Science Centre

Tadhunter C. et al., 2011, MNRAS, 412, 960

Telesco C. M. et al., 2003, in Masanori I., Alan F. M. M., eds, Proc. SPIE Conf. Ser. Vol. 4841, Instrument Design and Performance for Optical/Infrared Ground-based Telescopes. SPIE, Bellingham, p. 913
Toomre A., Toomre J., 1972, ApJ, 178, 623
Treister E., Schawinski K., Urry C. M., Simmons B. D., 2012, ApJ, 758, L39
Trippe M. L., Crenshaw D. M., Deo R., Dietrich M., 2008, AJ, 135, 2048
Tristram K. R. W. et al., 2009, A&A, 502, 67
Turner T. J., Weaver K. A., Mushotzky R. F., Holt S. S., Madejski G. M., 1991, ApJ, 381, 85
Usui T., Saito M., Tomita A., 1998, AJ, 116, 2166
Veilleux S., Shopbell P. L., Miller S. T., 2001, AJ, 121, 198
Weaver K. A., Nousek J., Yaqoob T., Mushotzky R. F., Makino F., Otani C., 1996, ApJ, 458, 160
Yaqoob T. et al., 2007, PASJ, 59, 283

This paper has been typeset from a TEX/LATEX file prepared by the author.